

NUMERICAL INVESTIGATION OF CAVITATING FLOW IN VARIABLE AREA
VENTURI ON THE BASIS OF EXPERIMENTAL DATA

A THESIS SUBMITTED TO
THE GRADUATE SCHOOL OF NATURAL AND APPLIED SCIENCES
OF
MIDDLE EAST TECHNICAL UNIVERSITY

BY

HASAN TOLGA GÜMÜŞEL

IN PARTIAL FULFILLMENT OF THE REQUIREMENTS
FOR
THE DEGREE OF MASTER OF SCIENCE
IN
MECHANICAL ENGINEERING

JANUARY 2020

Approval of the thesis:

**NUMERICAL INVESTIGATION OF CAVITATING FLOW IN VARIABLE
AREA VENTURI ON THE BASIS OF EXPERIMENTAL DATA**

submitted by **HASAN TOLGA GÜMÜŞEL** in partial fulfillment of the requirements
for the degree of **Master of Science in Mechanical Engineering Department,**
Middle East Technical University by,

Prof. Dr. Halil Kalıpçılar
Dean, Graduate School of **Natural and Applied Sciences**

Prof. Dr. M. A. Sahir Arıkan
Head of Department, **Mechanical Engineering**

Prof. Dr. M. Haluk Aksel
Supervisor, **Mechanical Engineering, METU**

Dr. Mehmet Ali Ak
Co-Supervisor, **Roketsan**

Examining Committee Members:

Assoc. Prof. Dr. M. Metin Yavuz
Mechanical Engineering, METU

Prof. Dr. M. Haluk Aksel
Mechanical Engineering, METU, METU

Prof. Dr. Kahraman Albayrak
Mechanical Engineering, METU

Assist. Prof. Dr. Ö. Uğraş Baran
Mechanical Engineering, METU

Assist. Prof. Dr. Onur Baş
Mechanical Engineering, TED University

Date: 06.01.2020

I hereby declare that all information in this document has been obtained and presented in accordance with academic rules and ethical conduct. I also declare that, as required by these rules and conduct, I have fully cited and referenced all material and results that are not original to this work.

Name, Surname: Hasan Tolga GümüŖel

Signature :

ABSTRACT

NUMERICAL INVESTIGATION OF CAVITATING FLOW IN VARIABLE AREA VENTURI ON THE BASIS OF EXPERIMENTAL DATA

Gümüsel, Hasan Tolga

M.S., Department of Mechanical Engineering

Supervisor: Prof. Dr. Mehmet Halûk Aksel

Co-Supervisor : Dr. M. Ali Ak

January 2020, 99 pages

Variable area cavitating Venturi is a throttling device that can regulate the flow rate used in liquid and hybrid rocket motors. It has a pintle mechanism which adjusts the flow area by moving back and forth in the direction parallel to the outflow from the Venturi. The flow rate is independent of the downstream pressure due to cavitation. This makes the variable area cavitating Venturi a very critical component for liquid propellant rocket engine because it can create an isolation between the inlet and the outlet in addition to controlling the mass flow rate. In this thesis, the cavitating flow through the variable area Venturi is investigated both experimentally and numerically. In order to solve the multi-phase flow, the open-source OpenFOAM software has been utilized. Schnerr-Sauer mass transport method is used to model the cavitation together with k-omega SST turbulence model. The model and the solver have tried to be verified and validated by experimental studies conducted on a simple version of the cavitating Venturi. The pintle positions, the upstream and downstream pressures, and the divergence angle of the Venturi has been examined in terms of their effect on the Venturi performance.

Keywords: Multi-phase Flow, Variable Area Cavitating Venturi, Computational Fluid Dynamics, Experimental, Fluid Mechanics

ÖZ

DEĞİŞKEN ALANLI VENTURİ'LERDE KAVİTASYONLU AKIŞIN DENEYSEL TEMELLİ NÜMERİK İNCELENMESİ

Gümüşel, Hasan Tolga

Yüksek Lisans, Makina Mühendisliği Bölümü

Tez Yöneticisi: Prof. Dr. Mehmet Halûk Aksel

Ortak Tez Yöneticisi : Dr. M. Ali Ak

Ocak 2020 , 99 sayfa

Değişken alanlı kavitasyonlu Venturi, özellikle sıvı ve hibrit yakıtlı roket motorlarında kullanılan akış kontrol bileşenlerindedir. Bu komponent kendi eksenine yönünde hareket ederek akış alanını ayarlayan bir mekanizmaya sahiptir. Venturi üzerinden geçen debi, kavitasyon etkisiyle çıkış basıncından bağımsız hale gelmektedir. Bu da değişken alanlı kavitasyonlu Venturiyi bir sıvı yakıtlı roket motoru için çok hayati bir bileşen yapar. Akış hızını düzenleme kabiliyetine ek olarak bu bileşen giriş ve çıkış hatları arasında bir izolasyon oluşturabilmektedir. Bu tezde, değişken alanlı Venturi içerisinde geçen kavitasyonlu akış, hem deneysel hem de sayısal olarak incelenmiştir. Çok fazlı akışı çözmek için açık kaynak kodlu OpenFOAM yazılımı kullanılmıştır. Kavitasyonu modellemek için Schnerr-Sauer kütle taşınım yöntemi, türbülans modellemek için ise k-omega SST türbülans modeli kullanılmıştır. Model ve çözücü, kavitasyonlu Venturinin basit bir versiyonunda yapılan deneysel çalışmalarla doğrulanmaya ve geçerlenmeye çalışılmıştır. Strok mesafesi, giriş ve çıkış basınçları ve Venturi çıkış açısı parametrelerinin Venturi performansına etkisi incelenmiştir.

Anahtar Kelimeler: Çok-Fazlı Akış, Değişken Alanlı Kaviteyonlu Venturi, Hesaplamalı Akış Dinamiği, Deneysel, Akışkanlar Mekaniği

To my family and Beyza

ACKNOWLEDGMENTS

I would like to express my deep gratitude to Professor M. Haluk Aksel and Dr. Mehmet Ali Ak, my thesis supervisors, for their patient guidance, support and useful critiques of this study. I would also like to thank Dr. Ahmet Sofyalı, for his advice and recommendations on this work.

I would also like to extend my thanks to Mr. Mehmet Can Köse and Mr. Erkan İlhan for their help in the experimental part of this study.

Finally, I wish to thank my parents and my girlfriend for their support and encouragement throughout my study.

TABLE OF CONTENTS

ABSTRACT	v
ÖZ	vii
ACKNOWLEDGMENTS	x
TABLE OF CONTENTS	xi
LIST OF TABLES	xv
LIST OF FIGURES	xvi
LIST OF ABBREVIATIONS	xx
CHAPTERS	
1 INTRODUCTION	1
1.1 General Information and Motivation	1
1.2 Literature Survey	4
1.2.1 Experimental Studies	4
1.2.2 Numerical Studies	7
1.3 OpenFOAM	9
1.4 Thesis Objective and Outline	10
2 VARIABLE AREA VENTURI AND CAVITATION	13
2.1 Design of Variable Area Venturi	13
2.2 Cavitation Phenomena	15

2.2.1	Schnerr-Sauer Cavitation Model	16
2.2.2	Zwart-Geber-Belamin Model	17
2.2.3	Full Cavitation Model	18
2.2.4	Barotropic Model	19
2.3	Limitations Through the Cavitation Models	20
3	EXPERIMENTAL STUDY	21
3.1	Experimental Conditions	21
3.2	Experimental Set-Up	22
3.3	Test Set-Up Components	25
3.3.1	Pressure Regulator	25
3.3.2	Pressure Transmitters	25
3.3.3	High Speed Camera	26
3.3.4	Turbine Type Flow-meter	27
3.4	Experimental Procedure	28
3.5	Test Results	29
3.5.1	Flow Visualization	29
3.5.2	Flow Measurement	31
4	NUMERICAL STUDIES	35
4.1	Governing Equations	36
4.2	CFD Model	37
4.2.1	OpenFOAM Solver	37
4.2.2	Turbulence Model	39
4.3	Validation Case	41

4.3.1	Geometry	41
4.3.2	Meshing	42
4.3.3	Boundary Conditions	44
4.3.4	Solver	45
4.3.5	CFD Result	51
4.3.5.1	Cavitation Mechanism Investigation	51
4.3.5.2	Effect of the Downstream Pressure on the Cavitating Flow	57
4.3.5.3	Effect of the Upstream Pressure on the Cavitating Flow	59
4.4	Variable Area Cavitating Venturi Case	62
4.4.1	The Geometry and Boundaries	63
4.4.2	CFD Results	65
4.4.2.1	Different Pintle Strokes	65
4.4.2.2	Effect of Downstream Pressure	69
4.4.2.3	Effect of Upstream Pressure	70
5	RESULTS AND DISCUSSIONS	73
5.1	Comparison of Experimental and Numerical Results	74
5.1.1	Mass Flow Rate Comparison	75
5.1.2	Oscillation Frequency	78
5.1.3	Cavitation Length	85
5.2	Variable Area Cavitating Venturi Case	87
5.2.1	Outlet Angle of the Venturi Investigation	89
5.2.2	Throat Length Investigation	89
5.2.3	Effect of Inlet/Outlet Pressure	90

5.2.4	Summary of the CFD Simulations	92
6	CONCLUSION&FUTURE WORK	95
	REFERENCES	97

LIST OF TABLES

TABLES

Table 3.1	Venturi Design Parameters	22
Table 3.2	Test Matrix	28
Table 4.1	Venturi Geometry used for the Validation	41
Table 4.2	Mesh Properties	43
Table 4.3	Types of BCs implemented in OpenFOAM	44
Table 4.4	Physical Properties of the Multi-Phase Flow at $20^{\circ}C$	45
Table 4.5	Time Step Independency	46
Table 4.6	The CFD Results	59
Table 4.7	The CFD Results	62
Table 4.8	The Design Parameters of the Variable Area Venturi	63
Table 5.1	Test Metrix	74
Table 5.2	The Fixed Area Cav.Venturi Simulation Matrix	75
Table 5.3	Frequency Results for Related Cases	85
Table 5.4	The Effect of the Outlet Angle	89
Table 5.5	Summary of Simulations Conducted	93

LIST OF FIGURES

FIGURES

Figure 1.1	Bi-propellant liquid rocket engine schematic	2
Figure 1.2	Combustion Chamber Pressure Varying with Time during Real Test [1]	3
Figure 1.3	Schematic of Venturi [4]	5
Figure 1.4	Schematic of experimental setup [4]	5
Figure 1.5	Mira 150 Engine Schematic	6
Figure 1.6	Schematic of variable area Venturi	7
Figure 1.7	General view of Variable Area Cavitating Venturi	11
Figure 2.1	Design Parameters of Variable Area Venturi	14
Figure 2.2	Distribution of Vapor Phase in Computational Domain[12]	16
Figure 2.3	Barotropic State Law $\rho(P)$ Water 20° C [19]	19
Figure 3.1	Venturi made from Plexiglass	22
Figure 3.2	Experimental Set-Up Schedule	23
Figure 3.3	A part of the Experimental Set-Up	24
Figure 3.4	Test Set-Up Data Acquisition System	24
Figure 3.5	Swagelok Pressure Regulator[24]	25

Figure 3.6	Flush Mounted Pressure Sensor [25]	26
Figure 3.7	High Speed Camera	26
Figure 3.8	Light Source and High Speed Camera	27
Figure 3.9	Turbine Type Flowmeter[26]	27
Figure 3.10	An Image of Cavitation Process	29
Figure 3.11	High Speed Camera Images for Cavitation Period	30
Figure 3.12	Measurement Results(Test No:3)	31
Figure 3.13	Measurement Results (Test No:2)	32
Figure 3.14	Measurement Results(Test No:6)	32
Figure 3.15	Spectrum of Pressure Oscillations	33
Figure 4.1	PIMPLE Algorithm Flow Chart [22]	38
Figure 4.2	Geometry of the Case Study	41
Figure 4.3	Mesh of Case Study	42
Figure 4.4	Viscous Sublayer Resolving Approach to resolve boundary layer (in red)[27]	43
Figure 4.5	Yplus for the Fixed Area Venturi	44
Figure 4.6	Mesh Independency Graph	45
Figure 4.7	Time Step Independency Graph	46
Figure 4.8	Number Density Effect on Liquid Volume Fraction	48
Figure 4.9	Number Density Effect on the Velocity Magnitude	49
Figure 4.10	Effect of the Number Density on Pressure Distribution along the Centerline of Venturi	50

Figure 4.11	Effect of the Number Density on Flow Rate	50
Figure 4.12	Liquid Volume Fraction at $t = 5.1$ ms	52
Figure 4.13	Static Pressure at 5.1 ms	52
Figure 4.14	Velocity Contour at $t = 5.1$ ms	52
Figure 4.15	Liquid Volume Fraction at yz plane at $t = 5.1$ ms	53
Figure 4.16	Static Pressure at yz plane at $t = 5.1$ ms	53
Figure 4.17	Velocity at yz plane $t = 5.1$ ms	54
Figure 4.18	Liquid Volume Fraction at yz plane at $t = 5.1$ ms	54
Figure 4.19	Liquid Volume Fraction vs. Time	55
Figure 4.19	Liquid Volume Fraction vs. Time	56
Figure 4.20	Typical Streamlines inside the Venturi	57
Figure 4.21	Effect of the Downstream Pressure on the Cavitation Length	58
Figure 4.22	Effect of the Downstream Pressure on Flow Oscillations	59
Figure 4.23	Effect of the Upstream Pressure on the Cavitation Length	61
Figure 4.24	Mass Flow Comparison for Different Upstream Pressure Values	62
Figure 4.25	The Geometry and Boundary Faces	64
Figure 4.26	Y-plus for Variable Area Venturi	64
Figure 4.27	Velocity Contours for Different Stroke Values	66
Figure 4.28	Pressure Contours for Different Stroke Values	67
Figure 4.29	Liquid Volume Fraction for Different Stroke Values	68
Figure 4.30	Mass Flow Rates for Different Stroke Values	69
Figure 4.31	Effect of the Downstream Pressure on the Cavitation Length	70

Figure 4.32	Effect of the Inlet Pressure on the Cavitation Length	71
Figure 5.1	Mass Flow Rate Comparison	76
Figure 5.2	The dimensional measurement of the tested Venturi	77
Figure 5.3	Mass Flow Comparison with 1.75 mm Thoroat Diameter Venturi	77
Figure 5.4	Mass Flow Rate vs Downstream Pressure(CFD Simulations) (Pinlet = 23 bara)	78
Figure 5.5	The CFD Simulation (Case 19)	79
Figure 5.6	The Flow Visualization (Case 7)	80
Figure 5.7	The CFD Simulation (Case 16)	81
Figure 5.8	The Flow Visualization (Case 8)	82
Figure 5.9	Mass Flow Rate vs Time (Case 16)	83
Figure 5.10	FFT of the Pressure Data (Case 7)	83
Figure 5.11	FFT of the Pressure Data (Case 9)	84
Figure 5.12	FFT of the Pressure Data (Case 10)	84
Figure 5.13	H.S.C. Image (Case 8)	86
Figure 5.14	CFD Simulation (Case 18)	87
Figure 5.15	Pintle Position vs Flow Rate Graph	88
Figure 5.16	Discharge Coefficient Based on CFD Simulations	88
Figure 5.17	No Throat Length Case	90
Figure 5.18	Mass Flow Rate vs. Time	91
Figure 5.19	Mass Flow Rate Comparison for Different Inlet Pressure	91
Figure 5.20	Discharge Coefficient vs Inlet Pressure	92

LIST OF ABBREVIATIONS

O/F ratio	Oxidizer to Fuel ratio
VACV	Variable Area Cavitating Venturi
CFD	Computational Fluid Dynamics
Re	Reynolds Number
Cd	Discharge Coefficient
σ	Cavitation number
A	Flow area
d_i	Inner diameter
d_o	Outer diameter
L	Length of truncated cone
θ	Pintle angle
x	Pintle position
R_t	Throat edge radius
ρ	Fluid density
P_1	Upstream Pressure
P_2	Downstream Pressure
P_v	Vapor Pressure
P_v	Vapor Pressure
ρ_m	Mixture density
ρ_v	Vapor density
ρ_l	Liquid density
μ_m	Mixture viscosity
μ_v	Vapor viscosity
μ_l	Liquid viscosity

μ_{eff}	Effective viscosity
Co	Courant number
CFL	Courant Friedrichs Lewy
3D	3 Dimensional
S_e	Eveporation source term
S_c	Condensation source term
n_0	Number density
α	Volume fraction of vapor
R_b	Bubble radius
C	Celsius

CHAPTER 1

INTRODUCTION

1.1 General Information and Motivation

In a Venturi, fluid flows through three cross sections successively, which are ordered as a linearly converging, a minimum area known as a throat and a linearly diverging. Such flow of both compressible and incompressible fluids is benefitted from in various engineering applications. If the Venturi used for incompressible fluids, cavitation is observed when the static pressure of the accelerated flow in the throat section becomes lower than its vapor pressure at the local temperature. The Venturi allowing the occurrence of this phenomenon is called the cavitating Venturi. Cavitating Venturi's have been used for years especially in mass flow measurements of fluids and in liquid propellant rocket engines. At this stage, it is better to explain the liquid propellant rocket engine in general.

Liquid-propellant rocket engines are aero-hydro-thermodynamic devices that convert chemical energy stored in liquid propellants into mechanical energy of the repelled combustion product mass. There are bi- and mono-propellant rocket engines. The main components of the system are propellant tanks, the combustion chamber, the nozzle, and the feeding system. Feeding systems can be of different types such as pressure-fed or turbo-pump-fed. Figure 1.1 is a simple diagram of a pressure-fed liquid propellant rocket engine. Turbo-pump-fed engines are relatively more complex. They will not be elaborated on this study.

In liquid propellant rocket engines, the fuel(F) and oxidizer(O) fill into the combustion chamber at a certain rate (O/F ratio) in order to have an efficient combustion and thereby maximize the specific impulse of the engine, which means minimizing

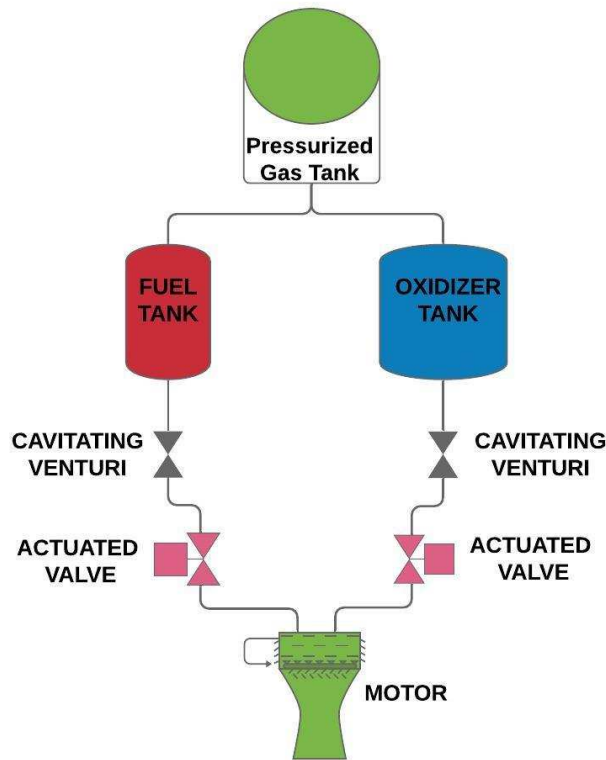


Figure 1.1: Bi-propellant liquid rocket engine schematic

the instantaneous propellant combustion needed to produce a desired constant thrust. This is achieved by the design of the feeding system. All components of the system are required to be characterized in terms of pressure loss and flow rate. In addition, since there is only ambient pressure in the combustion chamber at the starting phase of the engine, it is very important to prevent the fuel and oxidizer from reaching the combustion chamber in an uncontrolled manner, which may cause a so-called hard-start. Also, pressure oscillations in the combustion chamber, which affect the feeding system during operation of the engine, should be avoided. For these reasons, there is need for an isolation mechanism between the feeding system and the combustion chamber and also a flow limiter to sustain the O/F ratio. To emphasize pressure oscillations in the combustion chamber, a sample pressure distribution during combustion is shown in Figure 1.2.

For many years, cavitating Venturi has been utilized for the purpose mentioned above. The most important reason for using the cavitating Venturi in liquid rocket engines is

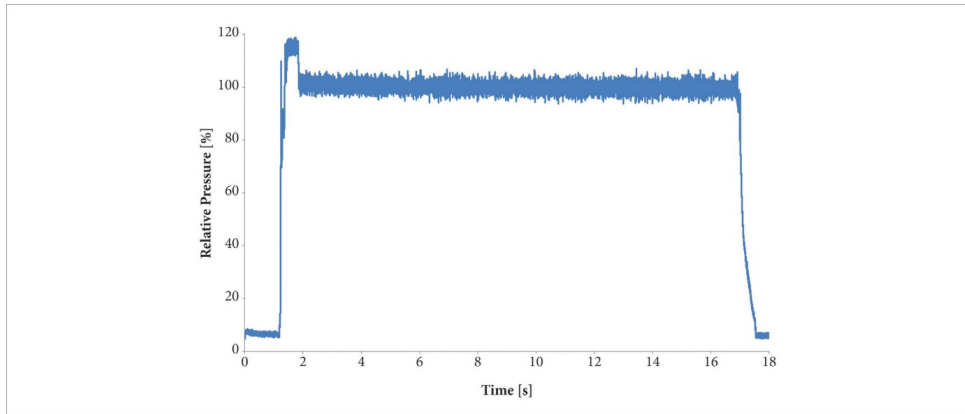


Figure 1.2: Combustion Chamber Pressure Varying with Time during Real Test [1]

its flow limitation property. The flow limitation occurring in a Venturi is due to the fact that bubbles formed as a result of cavitation. In other words, the multi-phase flow at the cavitation section, do not ultimately allow the mass flow to increase further. The liquid downstream rate becomes variant only if the downstream pressure gets higher than a certain value. In particular, the O / F ratio can be achieved by cavitating Venturi's placed just before the actuated valve. The most important feature of the cavitating Venturi used in liquid fuel rocket engines is to prevent transmitting the pressure fluctuations that may occur due to combustion instability to the upstream of the Venturi. This is called as the "choking phenomena"[2] . In this sense, cavitating Venturi provides an isolation function for the system. For similar purposes, cavitating Venturi's are also used in hybrid rocket engines.

The cavitating Venturi may be constant or variable flow area. Especially in liquid and hybrid (liquid+solid) propellant rocket engines, a variable flow area cavitating Venturi is employed to obtain variable thrust. In rocket motors with variable thrust profile is required, an advanced type of cavitating Venturi which regulates mass flow rate is also used. This device which allows an active flow control can be provided to operate the engine at the desired thrust level [3]. This actively controlled cavitating Venturi adjusts the mass flow by changing the flow area thanks to the back and forth movement of the pintle mechanism. In order to ensure that the flow rate remains constant without being affected by the changes in back pressure, cavitation is also desired.

On the other hand, one main disadvantage of cavitating Venturi is that there is a complex physical basis of its operation. The cavitating flow regime, in which phase transition, bubble formation and collapsing occur, is completely unstable. Regarding requirements of the Venturi element in terms of mass flow, pressure loss, total volume, maximum pintle stroke, the design and characterization of cavitating Venturi are highly difficult especially for its variable area type.

1.2 Literature Survey

There are many sources in the literature regarding the examination of the flow in a cavitating Venturi. These sources have been examined under two main titles as experimental and numerical studies.

1.2.1 Experimental Studies

Due to complex physics behind the flow through a Venturi, the characteristics of Venturi are mostly investigated experimentally. In this section, experimental studies related to the cavitating Venturi are presented.

Ghassemi, H., & Fasih, H. [4], have tested a Venturi having different throat diameters to evaluate dependence of performance on pressure of a fixed area cavitating Venturi. In this study, the performance range of the Venturi was determined at different inlet and outlet pressures. Also reaction of a Venturi to dynamically variable outlet pressure was examined. The results showed that different throat diameters had no effect on the performance of the cavitating Venturi and that the cavitating Venturi could maintain the same mass flow rate under variable outlet pressures. There is a technical drawing of the Venturi, which was tested, in Figure 1.3. In this work, experimental set-up (see Figure 1.4) has been built for the Venturi tests. At the end of the study, critical design parameters of the Venturi such as inlet and outlet angle, have been determined according to the given requirements.

Abdulaziz[5] modeled the effect of the vapor void ratio on the Venturi inlet-outlet pressure ratio in order to examine the vapor bubbles formed in the diverging section

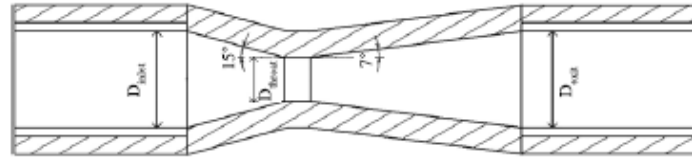


Figure 1.3: Schematic of Venturi [4]

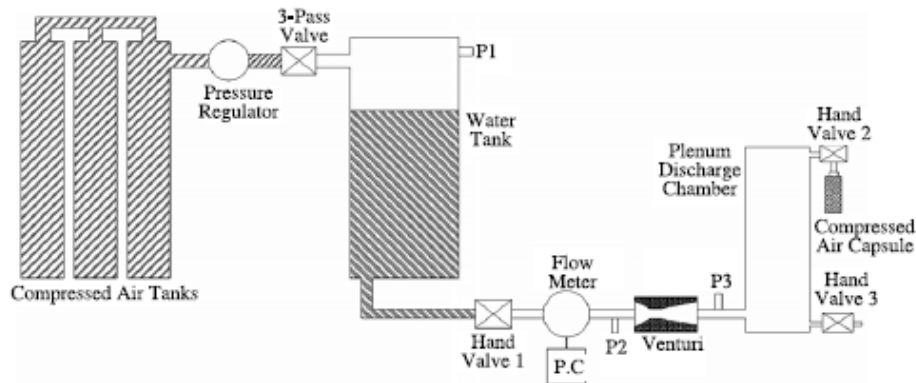


Figure 1.4: Schematic of experimental setup [4]

of the Venturi. Using the image processing method, the model was experimentally verified. In addition, the formation, transportation and collapse of the vapor bubbles were observed experimentally. Through all the conducted Venturi experiments, the critical pressure ratio ranges from 0.70 to 0.72 corresponding to a certain temperature.

Mena[6] has conducted research studies on the cavitating Venturi that can be used with cryogenic fluids in a Reaction Control System. As a result of these tests with cryogenic methane liquid and water, it was found that a Venturi can limit the flow up to inlet-outlet pressure ratios of 0.69.

All the above-mentioned studies were performed for fixed-area cavitating Venturi's. On the other hand, the earliest study for variable area cavitating Venturi is from D. Harvey [7]. In this study, the performance of adjustable Venturi valves used in Mira 150 Engine (see Figure 1.5) was investigated. Pintle contour design parameters were determined by analytical methods. A total of 62 flow characteristic test runs have been conducted and several cavitating and non-cavitating data points have been collected to determine the Variable Area Cavitating Venturi (VACV) characteristic. These test re-

sults show that a linear flow-position characteristic is attainable over a certain throttle range.

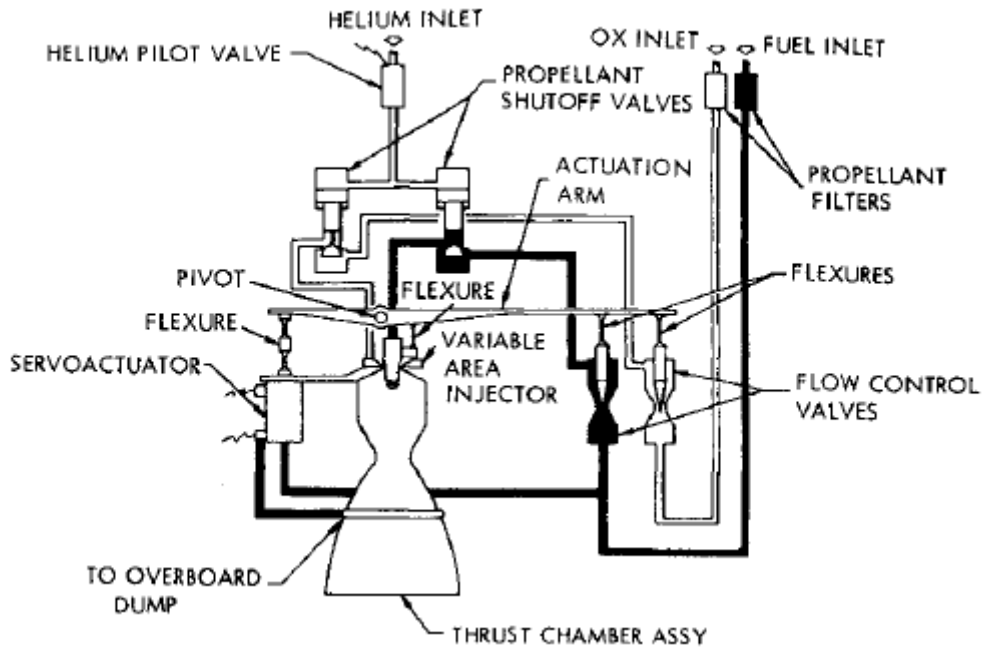


Figure 1.5: Mira 150 Engine Schematic

Tian[8], has designed and performed four different experiments to examine the performance of a cavitating Venturi with variable flow area to be used in Hybrid Rocket Engine (see Figure 1.6). He investigated the effect of parameters such as different pintle positions, inlet pressure, outlet pressure and dynamic movement of the pintle on the mass flow through the Venturi. Also, the change of discharge coefficient according to pintle positions and inlet and outlet pressures was examined. It was concluded that the effect of inlet and outlet pressure on the discharge coefficient was limited. As a result of the study, it was determined that the mass flow through the Venturi depends only on the pintle position and the inlet pressure. The tests were performed with equipment similar to the test set-up used by Ghassemi (see Figure 1.4).

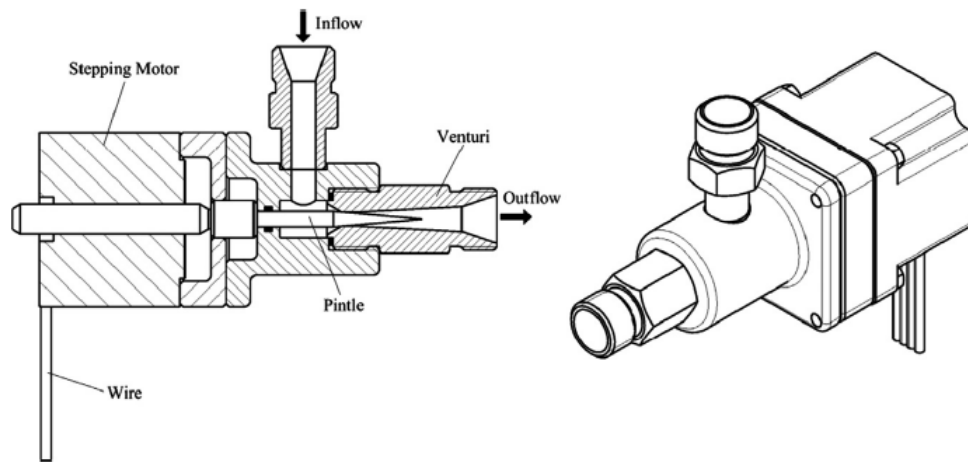


Figure 1.6: Schematic of variable area Venturi

1.2.2 Numerical Studies

Multidimensional modeling of cavitation flows is critical for the efficient design and performance of many engineering applications, including Venturi. There is a multi-phase flow due to cavitation at the divergent section of a Venturi. In order to understand the physics behind of the multi-phase flow, several numerical studies have been done. In this part, related works with the cavitation phenomena have been summarized.

Xu[9] simulated the cavitating flow in the Venturi using a homogeneous model. As a result of the calculations, it was observed that the bubbles formed in the throat were spread to the enlarged region and as a result, quasi-stable growth and collapse of bubble were observed. In this study, k-omega turbulence model was used. As a result of the study, it was stated that the multi-phase flow causes fluctuations on the flow rate. Also, mass flow variations of a 1–2% were demonstrated over a certain range of back-pressures for a venturi. It was also concluded that the cavitation oscillating frequency increased with decreasing cavitation number. Cavitation number is a dimensionless number which characterizes how close the pressure in the liquid flow is to the vapor pressure [10].

Goncalves [11] conducted numerical studies to model the cavitating flow. The study

was carried out on the effects of turbulence on multi-phase flow. Time dependent results were obtained for a Venturi geometry by using RANS and SIMPLE solver. The results were compared with the experiments and it was stated that the Menter SST model gave the closest results to the experimental data.

Schnerr-Sauer [12] developed a cavitation model by using modified Volume of Fluid (VOF) technique as well as modeling the bubble growth and collapse process. This process models the vapor distribution in a time-dependent solution set using void transport equations. In this study, unstable cavitating flow is modeled physically and numerically and compared with the tests performed. The physical model is considered as growth and collapse processes of vapor bubbles. The bubbles consist of structures already present in bulk fluid, called nuclei, whose growth and collapse depend on the surrounding environmental conditions. The assumption is that the nuclei are homogeneous, evenly distributed throughout the volume. It is also assumed that the bubble shape is spherical. The formation of cavitation actually involves phase transitions along with the multi-phase flow. In the case of entry and exit of the cavitation regime zones, the mixture density changes from the density of the pure liquid to a very low density, or vice versa. In order to overcome this discontinuous situation, the modified VOF technique was used based on the front capturing method in Schnerr-Sauer model. In this study, both phases are solved with the incompressible assumption. This model is explained in a detail way in the following sections.

Patella&Reboud[13] examined both experimental and numerically unstable cavitation for the Venturi section geometry characterized by a convergent angle of 18 degrees and a divergent angle of about 8 degrees. Highly accurate and reliable measurements for the flow rate, the void ratio and the instantaneous velocity fields in the Venturi were obtained. Two different homogeneous models, barotropic and void ratio transport models, were applied and compared. As a result of numerical studies, the unstable behavior of cavitation has been shown to be of good quality and acceptable accuracy for the both models. In addition, a global analysis of the cavitation cycle was performed and provided acceptable results were obtained. However, by performing a local and unsteady analysis of the void ratio and velocity fields, it was shown that there is no global agreement between all the computations done, mainly concerning void ratio distribution inside the cavitation region.

Zwart-Geber-Belamin presented a robust Computational Fluid Dynamics (CFD) methodology for 3D cavitating flow in their study[14]. In the developed model, multi phase flow equations and liquid-vapor continuity equations are taken as basis. The mass transfer rate is derived from the Rayleigh-Plesset equation. This model was applied to the commercial software CFX-5 program. The model was confirmed by various cavitating devices and different fluids. It was emphasized that the tests performed with Venturi and inducer could be simulated with the developed model.

In order to analyze the cavitating flow, Singhal has developed a so-called full cavitation model that takes into account the formation and transport of vapor bubbles, the pressure and velocity fluctuations in the low pressure zones, and the size of the dissolved and undissolved gases in the fluid [15]. The full cavitation model has been implemented into an advanced, general purpose, commercial CFD code, called CFD-ACE+. The model has been validated with the test results for flow over a hydrofoil, over a submerged cylindrical body, and flow in a sharp-edged orifice. Good agreement has been obtained in all cases without adjusting any coefficient values. For all simulations, the working fluid was water. Also, a second-order upwind scheme was used to discretize the convective fluxes, and turbulence was treated using the standard k-epsilon model.

The “Zwart-Geber-Belamin” and the “Full Cavitation Model” are examined in depth in upcoming sections.

Finally, Brinkhorst [16] conducted a numerical study for hydrodynamic cavitation in Herchel-Venturi tubes to be used for fluid flow measurement. Two and three dimensional cavitation simulation was performed using commercial software for two different nozzle geometries. It was stated that the total vapor volume ratio varies over time. However, it was found that this fluctuation had no effect on the stability of mass flow rate.

1.3 OpenFOAM

The name OpanFOAM comes from “Open Source Field Operation and Manipulation”. Based on C ++, this software is for numerical solvers and previous and post-

processing specializations for continuum mechanics and CFD problems. This software was first developed in Imperial College, London in the late 1980s. Mr. Hrvoje Jasak and Mr. Henry Weller are the two most important names in the development of OpenFOAM software. The code is provided free and open source under the GNU General Public License. The maintenance, management and distribution of the software is provided by the OpenFOAM organization, which is supported by volunteer participants [17].

OpenFOAM offers a robust and structured library of different solvers from financial evaluation analysis to CFD modeling. Like many other open source software, OpenFOAM lacks a user-friendly interface. On the other hand, it has a very powerful tool for CFD analysis. Due to the various advantages it provides, many industrial companies and engineers have started to use this software.

OpenFOAM provides comprehensive modeling capabilities for a wide range of incompressible and compressible, laminar and turbulent, single and multi-phase fluid flow problems. For a multi-phase flow solution, there are more than one solver in OpenFOAM. Various sources are available in the literature on solving multi-phase flows with OpenFOAM. As a result, in this thesis, OpenFOAM is used for CFD analysis of the cavitating flow.

In general about OpenFOAM; in this thesis, all words related to OpenFOAM are written in italic. All simulations were performed using OpenFOAM Windows version V1812. All units are SI.

1.4 Thesis Objective and Outline

In liquid propulsion systems, fixed-area cavitating Venturi's are used as a passive control element regardless of mono-propellant or bi-propellant. The flow through a Venturi is limited by the effect of the two-phase flow formed by the cavitation. In particular, uncontrolled accumulation of liquid in the combustion chamber and consequently the hard-start in the engine can be prevented by these Venturi's during the start of liquid propulsion system. However, the manufacturing of these fixed area cavitating Venturi's needs to be very precise and smooth. The parameters that are

very important for the system, such as discharge coefficient and pressure recovery, are directly related to the accuracy and tolerances in manufacturing. These situations both increase test costs and cause time loss. The use of variable-area cavitating Venturi will allow different flow rates to be obtained at constant inlet pressure. In this way, production errors on the Venturi can be tolerated. As a result, time and cost impact will be reduced.

In liquid propulsion systems, adjustable thrust is required for the a spacecraft during landing on earth, descending and remaining stable in space. In these systems, cavitating Venturi with adjustable flow area is used to complete the misson[3].

Moreover, since the product is subject to export license, it is very difficult to obtain it from overseas sources. Therefore, the design, production and characterization of a variable area cavitating Venturi to be used in a liquid propulsion system are to be carried out for the first time in Turkey. The cavitating Venturi with adjustable flow area is composed of a Venturi and a pintle mechanism as shown in Figure 1.7.

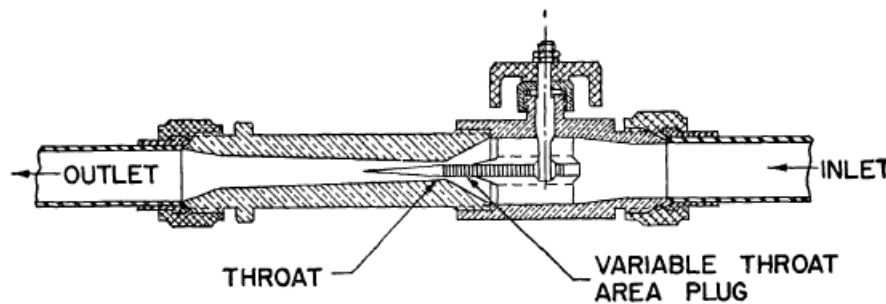


Figure 1.7: General view of Variable Area Cavitating Venturi

In the literature, although there are many studies on fixed area cavitating Venturi's, very few studies have been done on variable flow area cavitating Venturi's. Previously, ROKETSAN also carried out studies on fixed area cavitating Venturi's. For this reason, the design of the Venturi part for the variable area cavitating Venturi was made in accordance with the results of previous studies. However, both numerical and experimental studies are required to characterize the flow through the Variable Area Cavitating venturi (VACV). These studies will be realized within the scope of this thesis.

Numerical studies will be done using open source OpenFOAM software. ParaView software was used during the examination of the results of numerical studies. This program is also an open source. SALOME 8.0 software was used to create mesh. Again SALOME is also an open source.

As there is no general CFD code for analysing multi-phase flow, the results obtained from OpenFOAM will be verified both by comparison with existing literature and by using experimental data. The installation of the test equipment is carried out at ROKETSAN facilities. Since tests with liquid propellants are expensive and dangerous, all tests will be carried out with water. Accordingly, water is selected as the type of fluid in CFD analysis.

In the second chapter of the thesis, general flow equations and multi-phase models are explained. In addition, 1D analytical analyzes are performed. In Chapters 3 and 4, experimental and numerical studies of cavitating Venturi with variable flow area are provided, respectively. In Chapter 5, the results and comparisons are presented in tables. In Chapter 6, this study is concluded and related future work has been explained.

CHAPTER 2

VARIABLE AREA VENTURI AND CAVITATION

2.1 Design of Variable Area Venturi

As seen from Figure 2.1, the variable area Venturi composed of the Venturi which has convergent and divergent sections and pintle mechanism. The pintle is placed coaxially in the Venturi throat and moves back and forth through the Venturi. The flow area can be adjusted by changing the pintle position. Therefore, the mass flow rate of liquid has been controlled actively.

Flow area calculation based on geometrical manipulation has been done according to Figure 2.1. The details for obtaining a mathematical expression for the flow area is presented in the following.

$$A = \pi L \frac{(d_i + d_o)}{2} \quad (2.1)$$

where

$$L = x \sin \frac{\theta}{2} \quad (2.2)$$

$$d_o = d_t + 2|cd| \quad (2.3)$$

$$d_i = d_0 - 2|ae| \quad (2.4)$$

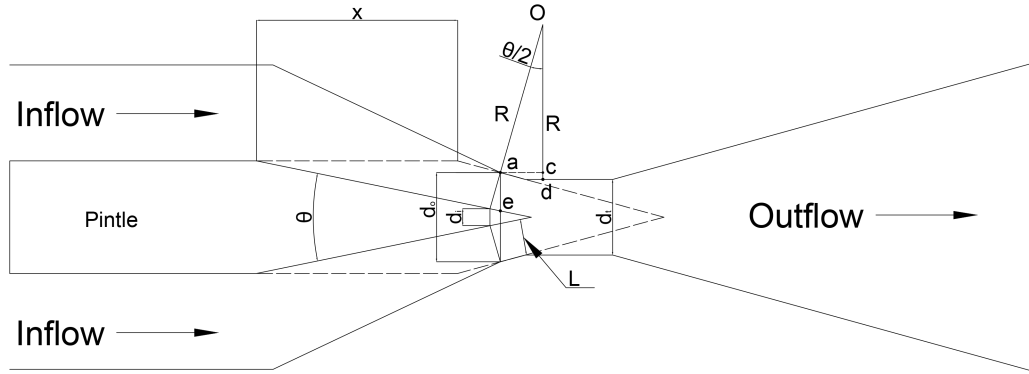


Figure 2.1: Design Parameters of Variable Area Venturi

$$|cd| = R - R \cos \frac{\theta}{2} \quad (2.5)$$

$$|ae| = x \cos \frac{\theta}{2} \quad (2.6)$$

Combining Equations (2.3) & (2.5);

$$d_o = d_t + 2R \left(1 - \cos \frac{\theta}{2} \right) \quad (2.7)$$

Combining Eqns. (2.4) & (2.6) & (2.7);

$$d_i = d_t + 2R \left(1 - \cos \frac{\theta}{2} \right) - 2x \sin \frac{\theta}{2} \cos \frac{\theta}{2} \quad (2.8)$$

Substituting Eqns. (2.7) & (2.8) into (2.1);

$$A = \pi x \sin \frac{\theta}{2} (d_t + 2R(1 - \cos \frac{\theta}{2})) - x^2 \sin^2 \frac{\theta}{2} \cos \frac{\theta}{2} \quad (2.9)$$

Using Bernoulli equation, the theoretical mass flow rate through the cavitating Venturi can be written as [8];

$$\dot{m} = A \sqrt{2\rho(P_1 - P_v)} \quad (2.10)$$

where \dot{m} is the mass flow rate, A is the flow area, P_1 is the upstream pressure and P_v is the vapor pressure of the fluid.

The above expression for the mass flow rate is based on inviscid and one-dimensional flow assumption. On the other hand, in the real case, actual flow area is smaller than the calculated flow area because of vena contracta. The ratio of the theoretical and actual flow areas is called discharge coefficient. This coefficient is depending on Reynolds number and geometry. It cannot be calculated from the one dimensional equation. It will be determined after numerical and experimental investigations.

2.2 Cavitation Phenomena

Cavitation is a phenomenon known as the formation of vapor bubbles in liquid structured flows due to the local static pressure falling below the vapor pressure. In the bulk liquid, there are some impurities called “nuclei”. As a result of the decrease in static pressure at constant temperature, these nuclei are transformed from microscopic size to macroscopic bubbles. When they reach a relatively high pressure zone, these bubbles collapse and generate intense shock waves[18]. These shock waves can cause serious damage in many engineering applications. However, knowing where cavitation will occur and controlling cavitation allows us to benefit from cavitation in some applications. Generally, a dimensionless parameter called cavitation number is

used for cavitation characterization as:

$$\sigma = \frac{P_1 - P_v}{P_1 - P_2} \quad (2.11)$$

where P_1 and P_2 are the upstream and downstream pressures, respectively.

Various studies have been conducted about how the cavitation can be modeled. Some of these studies were provided in the literature review part of the first chapter. In this section, detailed explanation of the cavitation models developed will be realized.

2.2.1 Schnerr-Sauer Cavitation Model

In this mass transfer based model, the modified Volume of Fluid is used for simulating the multi-phase flow. In the case of cavitation, the vapor bubbles and hence the vapor fraction are homogenously distributed in the computational cell. To illustrate the difference between standard and modified VOF methods, Figure 2.2 is presented. In cavitation process, the bubbles grow and collapse in addition to convective transport. The bubble geometry is assumed as sphere.

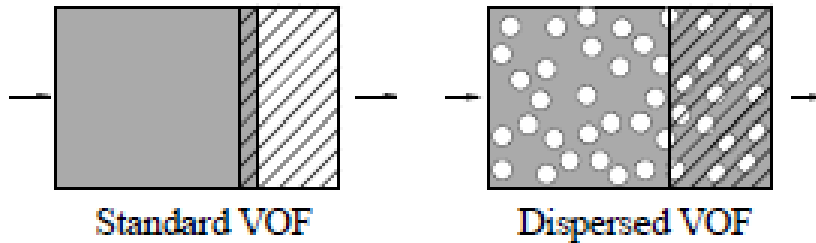


Figure 2.2: Distribution of Vapor Phase in Computational Domain[12]

Here, mathematical background for the density of the mixture when vapor and liquid densities are taken as constant can be given as follows:

$$\rho_m = \alpha\rho_v + (1 - \alpha)\rho_l \quad (2.12)$$

where ρ_m , ρ_l and ρ_v are densities of the mixture, liquid and vapor, respectively.

α is volume fraction of vapor and can be given by;

$$\alpha = \frac{V_v}{V_v + V_l} = \frac{n_0 V_l \frac{4}{3} \pi R_b^3}{V_l + n_0 V_l \frac{4}{3} \pi R_b^3} \quad (2.13)$$

where V_v and V_l are volume of liquid and vapor respectively, n_0 is the number density.

In the vapor transport equation, vapor generation is represented as source terms which are the evaporation and condensation rates.

$$\frac{\partial(\rho_v \alpha)}{\partial t} + \nabla \cdot (\rho_v \alpha u) = S_e + S_c \quad (2.14)$$

For simulating the bubble dynamics, Rayleigh-Plesset Equation is used with the simplifications[12]. So bubble radius growth rate is written as:

$$\dot{R}_b = \sqrt{\frac{2}{3} \frac{P_v - P}{\rho_l}} \quad (2.15)$$

where P is the local static pressure.

Combining Eqns. (2.12)(2.13)(2.14)and(2.15) with the continuity equation for fluid mixture, source terms obtained are given below.

$$S_c = \frac{\rho_l \rho_v}{\rho_m} \frac{3}{R_b} \left(\frac{2}{3} \frac{P - P_v}{\rho_l} \right)^{1/2} (1 - \alpha) \alpha \quad (2.16)$$

$$S_e = \frac{\rho_l \rho_v}{\rho_m} \frac{3}{R_b} \left(\frac{2}{3} \frac{P_v - P}{\rho_l} \right)^{1/2} (1 - \alpha) \alpha \quad (2.17)$$

2.2.2 Zwart-Geber-Belamin Model

This model is also based on mass transport of vapor. The same technique with the Schnerr-Sauer is used to model cavitation flow. The main difference is the equation

for the volume fraction of vapor which is given in as [14].

$$\alpha = n_0 \frac{4}{3} \pi R_b^3 \quad (2.18)$$

Gathering equations (2.12)(2.14)(2.15) and 2.18, the mass transfer rate due to cavitation per unit volume is obtained as:

$$S_c = C_c \frac{3\alpha\rho_v}{R_b} \sqrt{\frac{2}{3} \frac{P_v - P}{\rho_l}} \quad (2.19)$$

$$S_e = C_e \frac{3\alpha(1 - \alpha)\rho_v}{R_b} \sqrt{\frac{2}{3} \frac{P - P_v}{\rho_l}} \quad (2.20)$$

where C_e and C_c are the evaporation and condensation emprical constants.

2.2.3 Full Cavitation Model

In this model, as being a different from above two models, the relative velocity between liquid and the bubble is considered. Also, in this model instead of volume fraction, mass fraction term is used for the vapor. For bubble radius, a different correlation is used [15]. As a result, mass transport source terms are expressed below as:

$$S_e = C_e \frac{\sqrt{k}}{\sigma} \rho_l \rho_v \left(\frac{2}{3} \frac{P_v - P}{\rho} \right)^{1/2} (1 - f_v - f_g) \quad (2.21)$$

$$S_c = C_c \frac{\sqrt{k}}{\sigma} \rho_l \rho_l \left(\frac{2}{3} \frac{P - P_v}{\rho} \right)^{1/2} f_v \quad (2.22)$$

where f_v and f_g are vapor and gas mass fractions, σ is the surface tension, k is the turbulence kinetic energy and ρ is the mixture density here.

2.2.4 Barotropic Model

In this model, the cavitating flow is physically evaluated as a single liquid including compressibility effect. In the computational domain, the density of the fluid is determined by the barotropic state law, which establishes an equation between local static pressure and density. If the pressure in the cell is higher than the vapor pressure i.e. ($P > P_v + (\Delta P_v/2)$), the fluid is assumed to be completely liquid. On the other hand, if the pressure in the cell is much lower than the vapor pressure i.e. ($P < P_v - (\Delta P_v/2)$), the entire fluid in the cell is considered vapor and its density is determined by the perfect gas law. However, if the static pressure is close to the vapor pressure i.e. ($P_v + (\Delta P_v/2) < P < P_v - (\Delta P_v/2)$), this time the fluid consists of a mixture of liquid and vapor. The density of this mixture was determined by using barotropic law. Figure 2.3 is a visual representation of the barotropic model of water at 20° C [19]. The vapor ratio of the mixture is calculated as:

$$\alpha = \frac{\rho - \rho_l}{\rho_v - \rho_l} \quad (2.23)$$

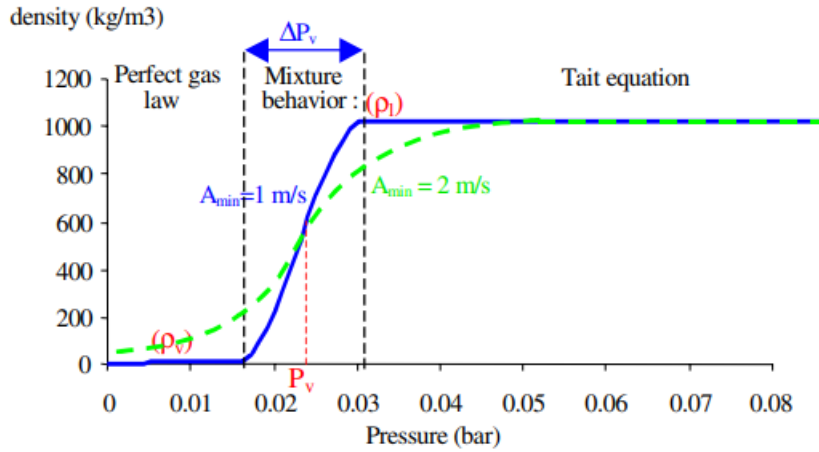


Figure 2.3: Barotropic State Law $\rho(P)$ Water 20° C [19]

The barotropic model can easily be integrated into CFD codes to be used to solve cavitating flows. However, since this model uses the assumption of thermodynamic equilibrium, it may be insufficient for the simulation of transient cavitation. Since it is assumed that the bubbles suddenly come into equilibrium as the flow conditions

change, bubble dynamics are not included to this model.

2.3 Limitations Through the Cavitation Models

All of the above mentioned cavitation models have some limitations. These limitations can be listed as follows [20], [21]:

- All cavitation models are valid for only one single fluid.
- Full cavitation model does not work with Large Eddy Simulation turbulence models.
- Full cavitation model may have convergence problems.
- Schnerr-Sauer, Zwart-Geber-Belamin and Barotropic models do not take non-condensable gas effects into considerations.
- Barotropic model does not take effect of bubble dynamics into account.
- Schnerr-Sauer, Zwart-Geber-Belamin and Barotropic models can not be used with slip velocities (for the interphase between vapor and liquid).
- Schnerr-Sauer and Zwart-Geber-Belamin are more robust models.

CHAPTER 3

EXPERIMENTAL STUDY

In this part of the study, it is aimed to obtain the flow characteristics of the fixed area cavitating Venturi in different conditions by using experimental methods. The cavitating flow which has complex physics was examined in detail using different test techniques. The main factors that affect the flow characteristics are determined by the tests to be performed under different boundary conditions.

Although performing tests takes a lot of time and is expensive, it is essential to verify and validate the CFD analyses. Consequently, the validated analysis can be used to perform new Venturi design activities. Pressure and flow properties were measured during the tests. In addition, flow visualization techniques were used to capture the phenomenon of cavitation. The purpose of this study is to design a variable area cavitating Venturi with validated analyzes using the data to be obtained during the experimental study.

Details of the test setup, test conditions and data acquisition system are given in the following sections.

3.1 Experimental Conditions

The use of propellant pairs used in liquid fuel rocket engines would be a very risky due to the possibility of explosion and firing during the tests to be performed within the scope of this study. For this reason, water was used as the working fluid throughout the tests. During the tests, Venturi's made from stainless steel and plexiglass were both used. The design parameters of both Venturi's are the same. Transparent Venturi

made of plexiglass were subjected to strength test in a safe environment before being used in the tests. In addition, a surface polishing process was also carried out after machining of Venturi to increase the visibility of the transparent Venturi (Figure 3.1). The each test was performed in 5 to 15 second intervals. Controlled filling of the tanks was performed before the test. The storage tank volume is 20 liters.

The design parameters of the produced Venturi are presented in Table 3.1.

Table 3.1: Venturi Design Parameters

Parameter	Value
Inlet Angle	15 degree
Outlet Angle	7 degree
Throat Diameter	1.68 mm



Figure 3.1: Venturi made from Plexiglass

3.2 Experimental Set-Up

A test set-up was built to perform cavitating Venturi tests. A simple version of the test apparatus is presented in Figure 3.2. In these tests, it is aimed to take pressure measurements at Venturi inlet and outlet in addition to flow rate in the hydraulic line. Also, a data acquisition system has been employed to collect data from the sensors used in the set-up.

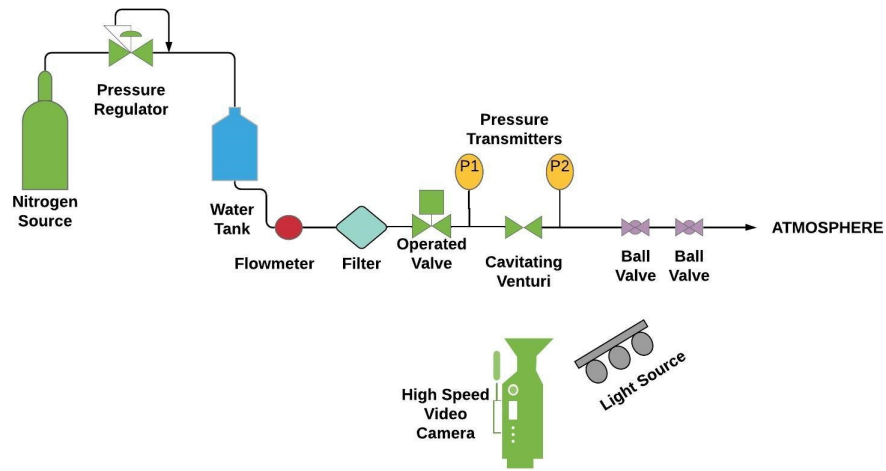


Figure 3.2: Experimental Set-Up Schedule

This test setup was made considering the structure of the pressure-fed liquid fuel engine in order to have similar system conditions. The system is based on the transfer of the pressure from gas to the water in the tank by the regulated compressed gas from a high pressure source and as a result the flow occurs due to the pressure difference. There is one pressure regulator in the system. The task of this regulator is to supply the gas in the high pressure nitrogen source to the system at a constant pressure. Thanks to the pressure regulator, the pressure in the tank remains constant throughout the flow. The liquid stored in the tank is controlled by the operated valve in the system. In addition, there is a 40 micron filter to prevent foreign particles in the system not to disturb the flow. Two ball valves are installed at the Venturi outlet to allow testing of the Venturi under different boundary conditions. It is possible to apply different Venturi outlet pressures by changing the flow area of these valves.

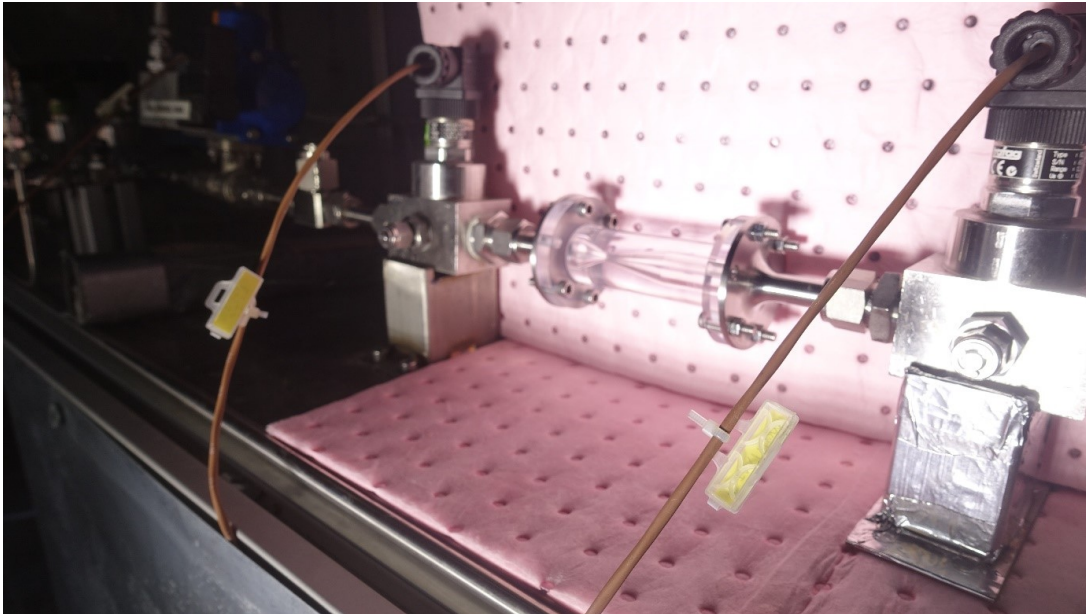


Figure 3.3: A part of the Experimental Set-Up

The system has a high speed camera and a light source to make visual observations. In particular, a powerful light source is needed to be able to capture images from the camera at high speed. The camera can also be activated by a computer. The resulting images are also recorded on this computer.

The data acquisition system is composed of National Instruments equipment (see Figure 3.4). The data was saved to the computer using NI Lab-View software. Also operated valve commands are also given through this software.

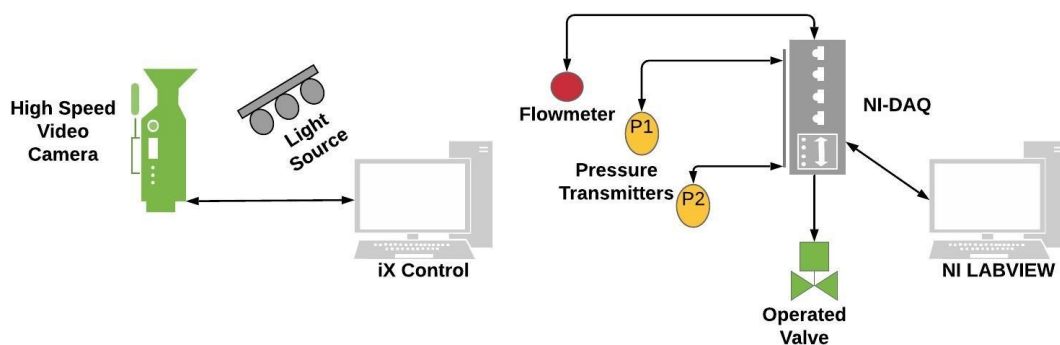


Figure 3.4: Test Set-Up Data Acquisition System

3.3 Test Set-Up Components

3.3.1 Pressure Regulator

Pressure regulator is a key component for pressure-fed liquid propellant rocket engine. In this test set-up, an industrial type pressure regulator is used. It can regulate high inlet pressures up to 413 bar. The pressure control range is 0 to 68.9 bar. It is appropriate for high flow applications. There is a visual, which belongs to pressure regulator, in Figure 3.5.



Figure 3.5: Swagelok Pressure Regulator[24]

3.3.2 Pressure Transmitters

The piezo-resistive type pressure sensors are used in this test set-up. They work with reference measurement principle. The measuring range is 0-100 bar. The accuracy is %0.4 at full scale.



Figure 3.6: Flush Mounted Pressure Sensor [25]

3.3.3 High Speed Camera

High Speed Camera is capable of shooting at high resolution and high frequency. The speed of shooting is up to 500 000 fps. However, the higher the shutter speed, the shorter the total time it can record. In the tests performed, images were taken at 20 000 fps and 1064x762 resolution. Also, when the frequency of shooting is increased, the camera needs more light. Therefore, a light source is used with the camera. There are two images related with these devices below.



Figure 3.7: High Speed Camera



Figure 3.8: Light Source and High Speed Camera

3.3.4 Turbine Type Flow-meter

In this set-up, turbine type flow meter is used in order to measure the flow rate at any instant of time. This type flow meter measures volumetric flow rate and is used for incompressible applications. There is a turbine which has six blades in this sensor. When the flow starts, the turbine starts spinning. The blades on it create pulses as they pass through the magnetic field inside the sensor. The number of these pulses are calibrated and instantaneous flow rate is measured.



Figure 3.9: Turbine Type Flowmeter[26]

3.4 Experimental Procedure

Several tests are conducted to obtain Venturi characteristics which are listed Table 5.1. Tests were performed at the same inlet pressure but at different outlet pressures to determine whether the flow through the Venturi was independent of the outlet pressure or not. In addition, tests were carried out at different inlet pressures to obtain the flow as a function of the inlet pressure. In addition, in order to determine the cavitation pressure ratio of the Venturi, the test was carried out at variable outlet pressure by manipulating the position of the ball valves at the Venturi outlet.

Table 3.2: Test Matrix

Test Number	Inlet Press.[barg]	Outlet Press.[barg]	Temp.[° C]
1	23	4	20
2	23	6	20
3	23	8	20
4	23	10	20
5	23	12	20
6	23-20	Dynamic	20
7	27.5	2	20
8	27.5	4	20
9	27.5	8	20
10	17.5	2	20
11	25	4	20

All tests are planned to last for 5 to 15 seconds. They are performed under constant temperature. In addition, a high speed camera images were taken during the first 5 tests in the test matrix table. During the test, the sampling frequency was 4000 Hz. In order to investigate the sensor data, Fast-Fourier Transform and moving average filter have been applied.

3.5 Test Results

In this section, the fixed area cavitating Venturi test results are presented. Throughout the tests, the effects of the inlet and outlet pressures have been investigated by using visualization and measurement techniques. Also, the inlet/outlet pressure ratio where the cavitation starts has been obtained.

3.5.1 Flow Visualization

In order to observe the cavitation phenomena, the transparent Venturi has been used. During these tests, images have been taken by using high-speed camera. An image related to the cavitation process is presented in Figure 3.10.

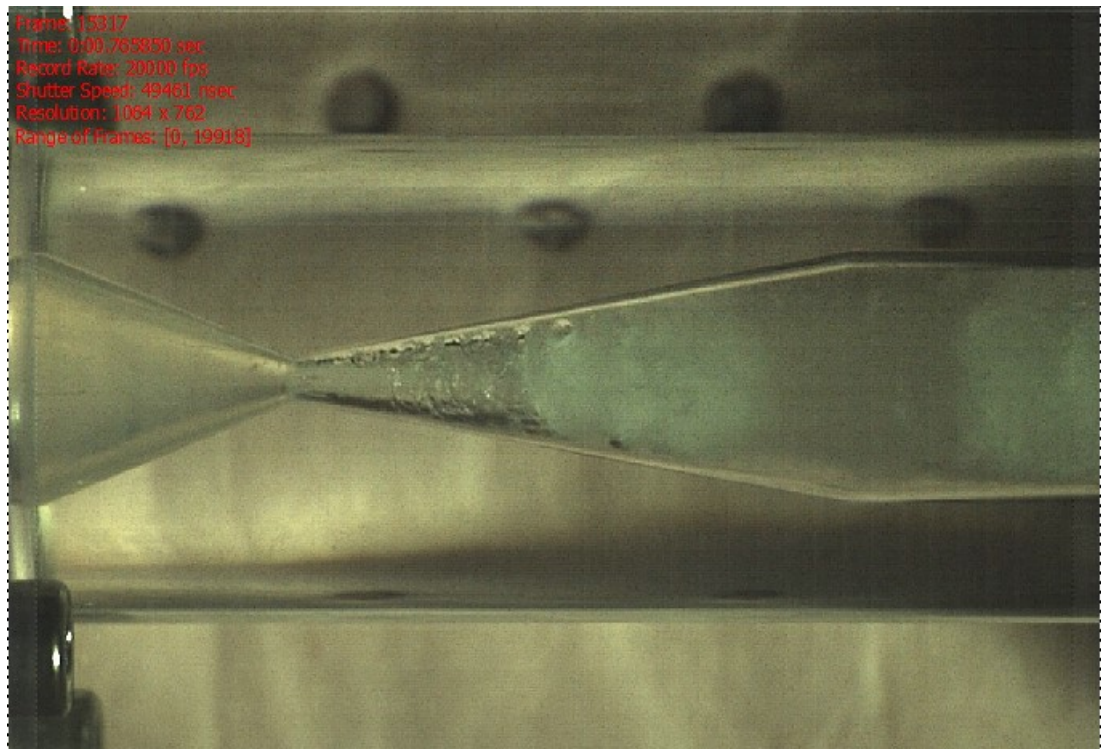


Figure 3.10: An Image of Cavitation Process

The left section is the inlet and the right section is the outlet part of the transparent Venturi. Bubbles can be seen easily from the image. They start from throat section and continue in the divergent part. They go almost up to end of the Venturi. The

bubble formation and collapsing process occurs within a certain period. Nevertheless, this process takes place in a very short time that cannot be detected by the human eye. In order to determine this period, the high speed camera images have been processed.

The images have been shown one by one in Figure3.11. As it can be seen, firstly the bubbles occur at the throat section of the Venturi. Next, they spread to the divergent part of the Venturi. When they reach a certain point, the bubbles start to collapse due to pressure recovery. Finally, they all collapse and start growing again from the throat. This process repeated in the same way.

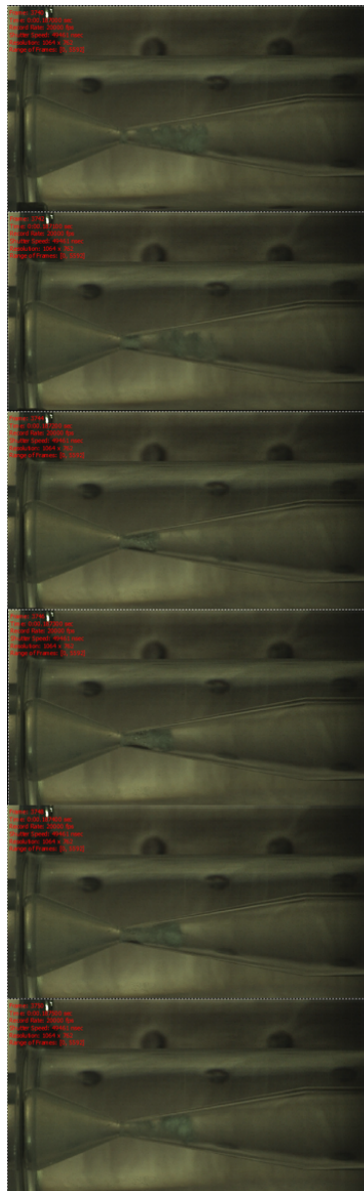


Figure 3.11: High Speed Camera Images for Cavitation Period

These tests have been conducted for different downstream pressure conditions. Detailed results have been presented in Chapter 5.

3.5.2 Flow Measurement

The flow properties through the Venturi has been measured by using pressure sensors and flow meter device. In this section, the measurement results have been examined.

In Figure 3.12, the measurements when the inlet and outlet pressures are constant are presented.

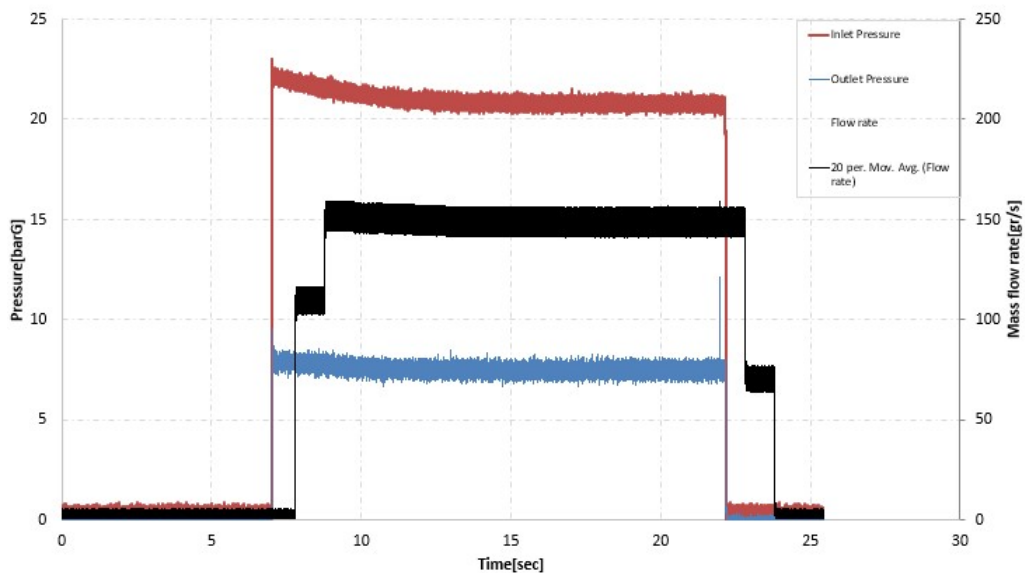


Figure 3.12: Measurement Results(Test No:3)

When the operated valve is energized, the pressure values start to rise up to certain value which can be seen from the figure above. Also, the flow rate readings are taken from the flowmeter. However, in this test there is a time shift between pressure sensor values and flowrate values. Turbine type flow meter could not give response fast enough. In addition, the data are quite noisy. Therefore, the average values are taken into considerations while examining the results.

In Figure 3.13, the measurements when the Venturi is under a lower downstream pressure conditions are presented.

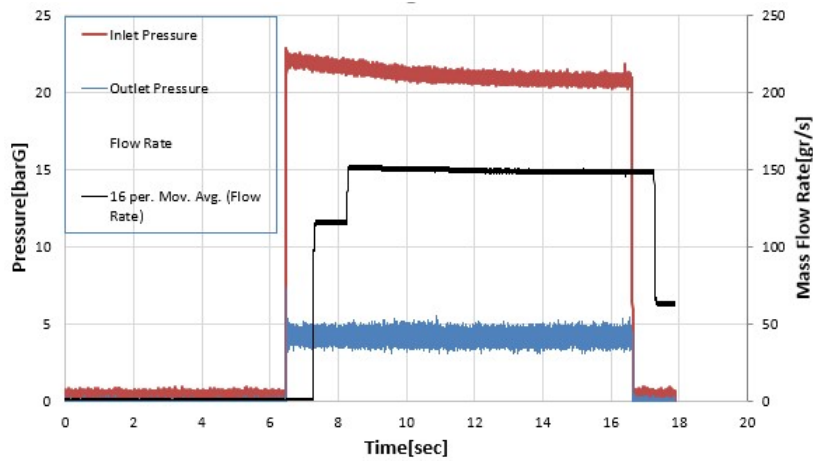


Figure 3.13: Measurement Results (Test No:2)

When the results presented in Figures 3.12 and 3.13, for which the same inlet conditions are applied, are compared, it is possible to observe that the average mass flow rates for these two cases are very close. Therefore, it can be said that the mass flow rate does not depend on the downstream pressure.

The dynamic downstream pressure case is also investigated in Figure 3.14.

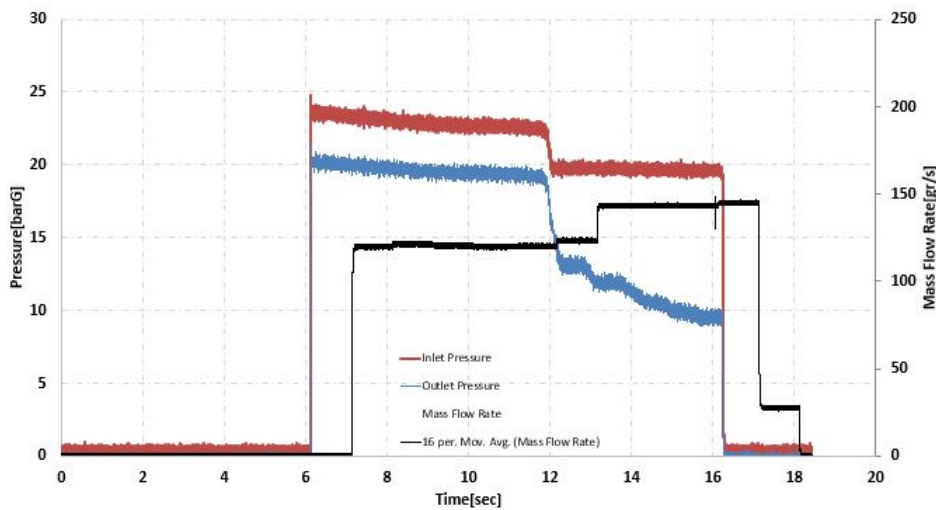


Figure 3.14: Measurement Results (Test No:6)

In test number 6, during the first half of the test, the decreasing inlet pressure did not affect the flow rate since the downstream pressure is decreasing at the same rate and,

thus, the pressure difference remains the same. Therefore, it can be concluded that the flow only depends on the outlet pressure and it does not cavitate. When the outlet pressure is decreased continuously at the second half of the test, it can be said that the cavitation starts since the flow rate did not increase anymore. In other words, the flow is choked.

In addition, in order to obtain flow oscillation frequency at the outlet of the Venturi, the fast fourier transform is applied to the pressure sensor data. In Figure 3.15, the dominating frequency can easily be seen.

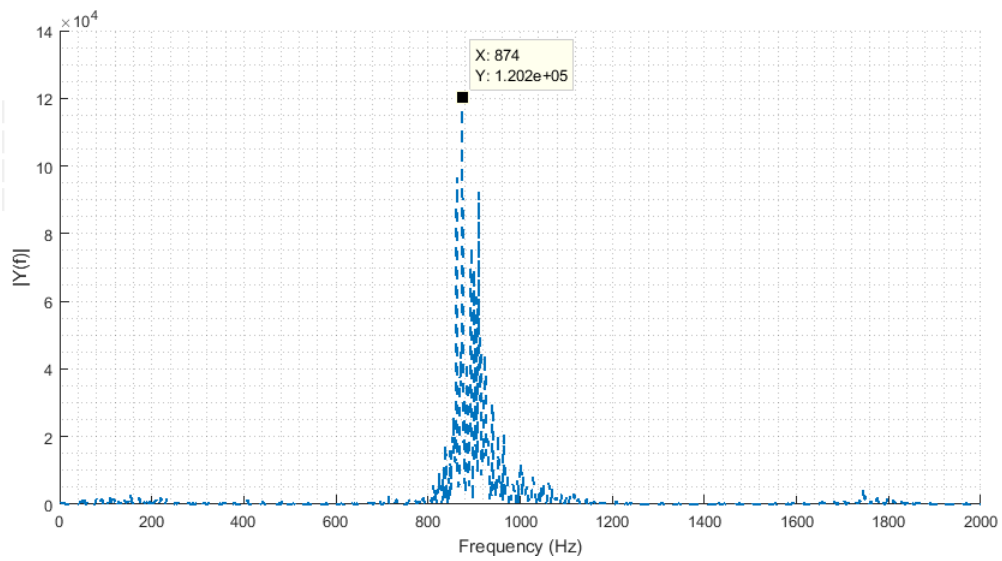


Figure 3.15: Spectrum of Pressure Oscillations

CHAPTER 4

NUMERICAL STUDIES

Until the early 2000's, experimental methods were used to develop systems containing cavitating flow by performing a large number of tests. However, in recent years, numerical methods have become a part of solution of multi-phase systems thanks to the increasing solution capacities with the emergence of models for the analysis of cavitating flows and the rapid development of computer technologies.

The main aims of using a numerical approach in this field are as follows:

- 1) To reduce the number of design iterations
- 2) To create the preliminary designs as a result of numerical studies
- 3) To make the highly accurate design of the test equipment as fast as possible by using a result of the predictions given by the numerical studies
- 4) To reduce the test cost and time, avoiding unnecessary tests,
- 5) To be able to improve numerical studies by using test data and use them in future design optimization stages.

Although there are many commercial software available today for numerical studies, the cost of these software is very high. Within the scope of this thesis, numerical studies were carried out by using open source software instead of using a commercial one. For this purpose, OpenFOAM, which is an open source, is used for CFD analysis. OpenFOAM has separate solvers for each type of a flow field, as well as multiple solvers for the solution of multi-phase flow. The meshing part of the numerical studies was carried out by using open source SALOME software. ParaView, another open source program, was used to obtain and evaluate the analysis outputs.

In this section, the methodology of numerical approach will be explained and information about OpenFOAM solvers will be given. In order to validate the solvers in OpenFOAM before using it for a variable area Venturi analysis, a fixed area cavitating Venturi is analyzed as a case study. This analysis has been compared with the experimental studies conducted in Roketsan premises. Then, a preliminary analysis of variable area cavitation Venturi was performed. In all CFD analysis, water is used as the fluid type.

4.1 Governing Equations

The two-phase cavitating flow is treated as a single fluid with homogeneous mixture approach. This approach provides the same velocity and same temperature for both two phases at the interfacial. In this model, both two phases are assumed to be incompressible. Also, since the temperature change has negligibly small effect on thermodynamic properties of fluids, the energy equation is not taken into account in the CFD analysis. For the cavitation modelling, the mass transport approach is used instead of the barotropic model because of the limitations of the model which is mentioned in Chapter 2.

Then, the governing equations consist of continuity, momentum equations for the mixture and a vapor mass transport equation for phase distribution model. They are all provided in following;

The density and viscosity for the mixture are given as follows:

$$\rho_m = \alpha\rho_v + (1 - \alpha)\rho_l \quad (4.1)$$

$$\mu_m = \alpha\mu_v + (1 - \alpha)\mu_l \quad (4.2)$$

The momentum, continuity and mass transport equations are provided below.

$$\frac{\partial \rho_m U}{\partial t} + \nabla(\rho_m U U) = -\nabla p + \nabla [(\mu_{eff}(\nabla U + (\nabla U)^T)) + f_\sigma] \quad (4.3)$$

$$\mu_{eff} = \mu_m + \mu_t \quad (4.4)$$

where μ_t is the turbulent viscosity.

$$\frac{\partial \rho_m}{\partial t} + \nabla(\rho_m U) = 0 \quad (4.5)$$

$$\frac{\partial(\rho_v \alpha)}{\partial t} + \nabla \bullet (\rho_v \alpha u) = S_e + S_c \quad (4.6)$$

where α is the vapor volume fraction, S_e and S_c are the evaporation and condensation source terms.

4.2 CFD Model

In this thesis study, all CFD analyzes are done for 3D case. Reynolds Averaged Navier-Stokes equations are solved by including the turbulence effects. Since there is no general code available for the cavitating flow, the model, which is used for simulating the flow, is verified with the help of the results in the literature and tests conducted at ROKETSAN. Throughout the verification, a fixed area cavitating Venturi is used due to existence of many test data. SALOME V8.0 software is utilized as the meshing tool. In this part, information related with the background about the CFD analysis is provided.

4.2.1 OpenFOAM Solver

In OpenFoam the Finite Volume Method is used to discretize the Navier-Stokes equations. The *interPhaseChangeFoam* solver is commonly used for multi-phase flow simulation. The solver is for two incompressible, isothermal immiscible fluids with phase change such as cavitation. It uses a modified VOF (Volume of Fluid) phase-fraction based interface capturing approach. This solver uses PIMPLE algorithm

which is combination of SIMPLE (Semi-Implicit Method for Pressure Linked Equations) and PISO (Pressure-Implicit with Splitting of Operators) for solving velocity and pressure. The PIMPLE flow chart can be seen in Figure 4.1.

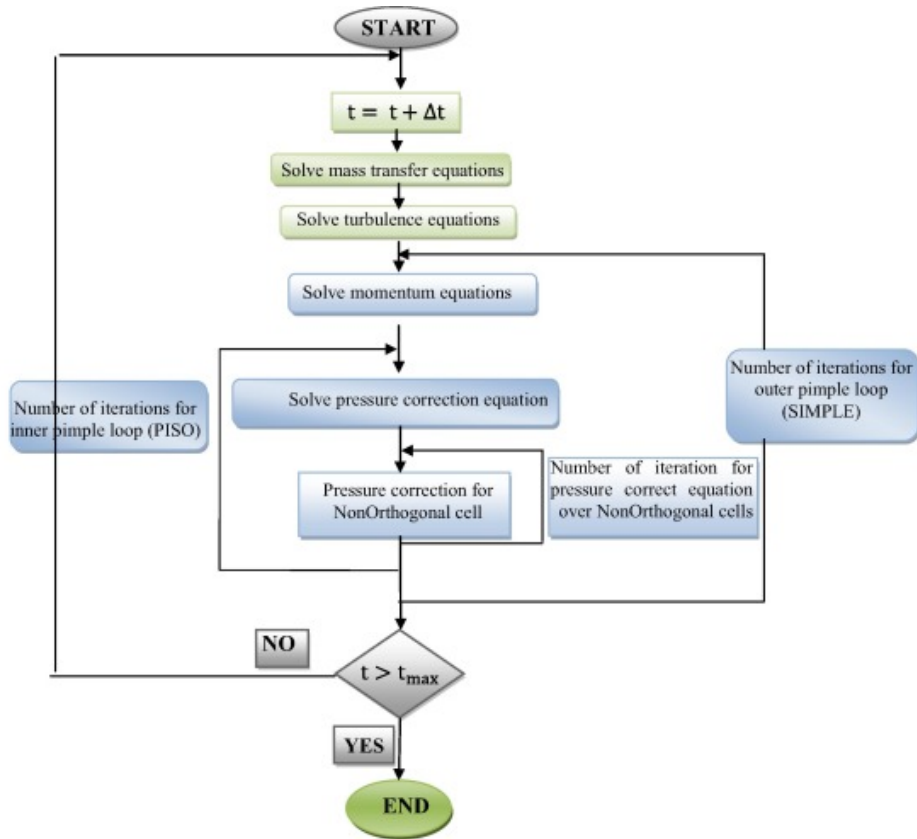


Figure 4.1: PIMPLE Algorithm Flow Chart [22]

By using PIMPLE algorithm, a more robust pressure-velocity coupling can be obtained. The algorithm can provide more stable results for larger Courant Numbers when it is compared with PISO algorithm [22].

In the OpenFOAM, the case folder consists of “0,” “constant” and “system” files. In the “0” which means initial time directory, initial and boundary conditions are designated. In the “constant” file, there are files specifying the physical properties for the application concerned and a full description of the case mesh file. Finally, setting parameters related with the solution procedure itself are found in the “system” directory.

The algorithm for the *interPhaseChangeFoam* solver is given below.

1. Read the control parameters
2. Calculate the mean and maximum Courant number
3. Adjust time step size according to Courant number
4. Enter into the PIMPLE Loop
5. In the PIMPLE Loop, read the control parameters for alpha equation. For solving alpha equation, MULES (Multidimensional Universal Limited Explicit Solver) is used.
6. Solve mass transport equation and obtain new distribution
7. According to the new distribution, obtain new mixture properties
8. Solve turbulence and momentum equations
9. Loop for the pressure correction
10. Check whether time has reached the maximum time or not
11. If not, go to Step 2 , if yes terminate.

4.2.2 Turbulence Model

All flows that exist in engineering applications become unstable when they exceed a certain Reynolds number. High Reynolds number appears to be turbulent. Completely chaotic and random state of motion is caused by time-dependent velocity and pressure changes. In many engineering problems, average flow behavior is dealt with. However, turbulence effects cannot be ignored since turbulence-induced flow fluctuations create extra Reynolds stresses on the mean flow and the extra stresses on this flow need to be modeled in the CFD. In OpenFOAM, there are many turbulence model options that can be chosen for different problems.

Turbulence effects should also be added to the cavitating flows which are quasi-stable in nature. In the literature, both *k-omega* SST and realizable *k-epsilon* models are used in CFD models of cavitating flows for different geometries. In this thesis, one of the Reynolds Averaged Navier Stokes turbulence models, *k-w* SST turbulence model was

applied. This model is two equation model for the turbulence kinetic energy, k , and turbulence specific dissipation rate, ω . It is developed for overcoming the deficiencies of the standard k - ω model with respect to dependency on the free stream values of k and ω . In the model, there is a function which blends effectively formulation of the k - ω model in the near-wall region and the k - ϵ model at the far field[23]. The model is capable of capturing flow separation.

The turbulence specific dissipation rate equation is given by:

$$\frac{D(\rho\omega)}{Dt} = \nabla(\rho D_\omega \nabla \omega) + \frac{\rho\gamma G}{\nu} - \frac{2}{3}\rho\gamma\omega(\nabla u) - \rho\beta\omega^2 - \rho(F_1-1)CD_{k\omega} + S_\omega \quad (4.7)$$

while the turbulence kinetic energy is as follows:

$$\frac{D}{Dt}(\rho k) = \nabla(\rho D_k \nabla k) + \rho G - \frac{2}{3}\rho k(\nabla u) - \rho\beta^* \omega k + S_k \quad (4.8)$$

The turbulence viscosity is obtained using:

$$\nu_t = a_1 \frac{k}{\max(a_1\omega, b_1 F_{23} S)} \quad (4.9)$$

For isotropic turbulence, the turbulence kinetic energy can be estimated initially by:

$$k = \frac{3}{2}(I|U_{ref}|)^2 \quad (4.10)$$

where I is the intensity, and U_{ref} is the reference velocity. The turbulence specific dissipation rate follows as:

$$\omega = \frac{k^{0.5}}{C_\mu L} \quad (4.11)$$

where C_μ is a constant equal to 0.09, and L is a reference length scale.

4.3 Validation Case

Fixed area cavitating Venturi simulation is taken as a validation case since there are lots of experimental results available in literature. 3D transient CFD analysis has been conducted on the flow through the cavitating Venturi. In this section, first the geometry of the case is shown. Then, the meshing of geometry is presented in a detail manner with all the meshing parameters. Next, the boundary conditions are explained. Finally, information about the OpenFOAM case such as solver type, Courant number, cavitation model type are provided.

A Venturi having 1.68 mm throat diameter has been chosen as a validation case. For a given set of boundary conditions, the mass flow rate and the effect of the upstream and downstream pressures on the flow will be determined.

4.3.1 Geometry



Figure 4.2: Geometry of the Case Study

The Venturi geometry is described in the Table 4.1.

Table 4.1: Venturi Geometry used for the Validation

Throat Diameter	1.68 mm
Inlet Angle	15 deg
Outlet Angle	7 deg
Pipe Diameter	10 mm

4.3.2 Meshing

The meshing is carried out by using Salome 8.0 software. As it can be seen from Figure 4.2, the cavitating Venturi has a circular cross-section. In order to make hexahedral meshing, a rectangular prism has been created in the Venturi geometry. Therefore, all blocks of the Venturi geometry have four edges for each face which are needed for hexahedral mesh.

As a final step, the created mesh are exported as “unv.” format which is compatible with OpenFoam.

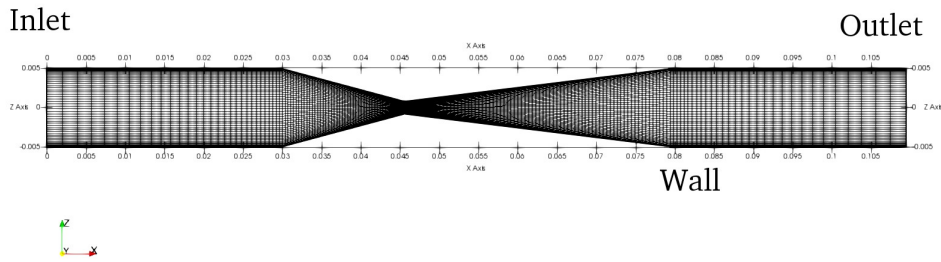


Figure 4.3: Mesh of Case Study

While meshing, a viscous layer has been generated near to the wall. In the variable area Venturi case, y^+ criteria has been checked between inlet and outlet of the geometry. y^+ can be kept approximately in the range of 30 to 50. Since the wall function is used y^+ can be greater than a certain value and coarser mesh can be applied to reduce computational time.

$$y_1 = \frac{y^+ \mu}{\sqrt{\rho \tau_w}} \quad (4.12)$$

where y_1 is the first layer thickness, μ is the dynamic viscosity of the fluid, ρ is the fluid density and τ_w is the wall shear stress.

In order to check mesh independency of the numerical model, the analyzes have been

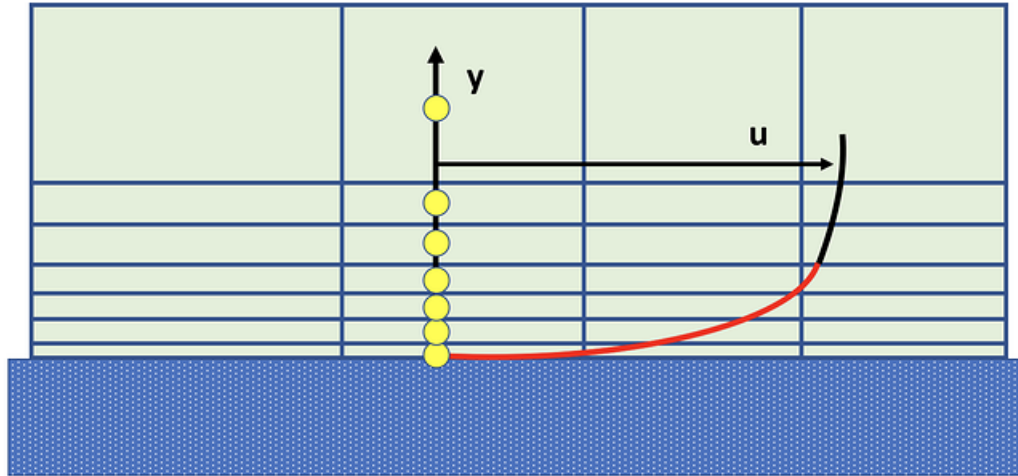


Figure 4.4: Viscous Sublayer Resolving Approach to resolve boundary layer (in red)[27]

carried out with four different meshes having different element size. The results are demonstrated in Table 4.2. Relative error between results are calculated according to the following equation.

$$\%Error = 100 \frac{Abs[(Result)_i - (Result)_{i+1}]}{(Result)_{i+1}} \quad (4.13)$$

Table 4.2: Mesh Properties

Index(i)	Mesh	Element Size	Mass Flow Rate[kg/s]	Rel. Error[%]
1	Coarse	127 680	0.106	19.18
2	Moderate	336 000	0.126	4.52
3	Fine	652 500	0.130	1.38
4	Very Fine	1 080 000	0.131	-

As seen from Figure 4.6, the results are getting independent of the mesh size after a mesh having 600 000 elements. It is not necessary using very fine mesh due to the computational cost. From this point, all the analyzes have been conducted by using fine mesh.

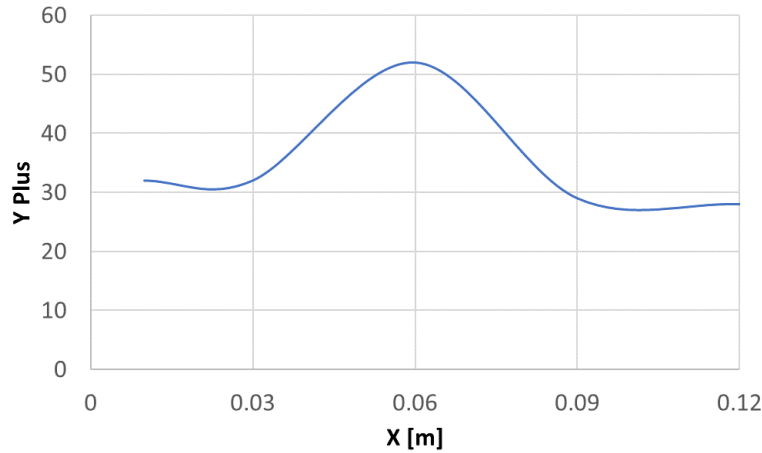


Figure 4.5: Yplus for the Fixed Area Venturi

4.3.3 Boundary Conditions

All boundary and initial conditions are provided in “0” file in OpenFOAM. In the validation case, the OpenFOAM boundary types are summarized in Table 4.3. For the inlet boundary conditions, total pressure is defined. The outlet boundary condition is fixed static pressure. No slip condition is applied at the wall. Also, for the inlet and outlet, vapor ratio is defined as 1.

Table 4.3: Types of BCs implemented in OpenFOAM

Boundary Types				
Patches	alpha.water	Pressure	Velocity(Ux,Uy,Uz)	rho
Inlet	<i>fixedValue</i>	<i>totalPressure</i>	<i>zeroGradient</i>	<i>fixedValue</i>
Outlet	<i>inletOutlet</i>	<i>fixedValue</i>	<i>inletOutlet</i>	<i>fixedValue</i>
Wall	<i>fixedValue</i>	<i>zeroGradient</i>	<i>noSlip</i>	<i>zeroGradient</i>

Physical properties for the multi-phase flow are given in “constant” file in OpenFOAM and these are presented in Table 4.4.

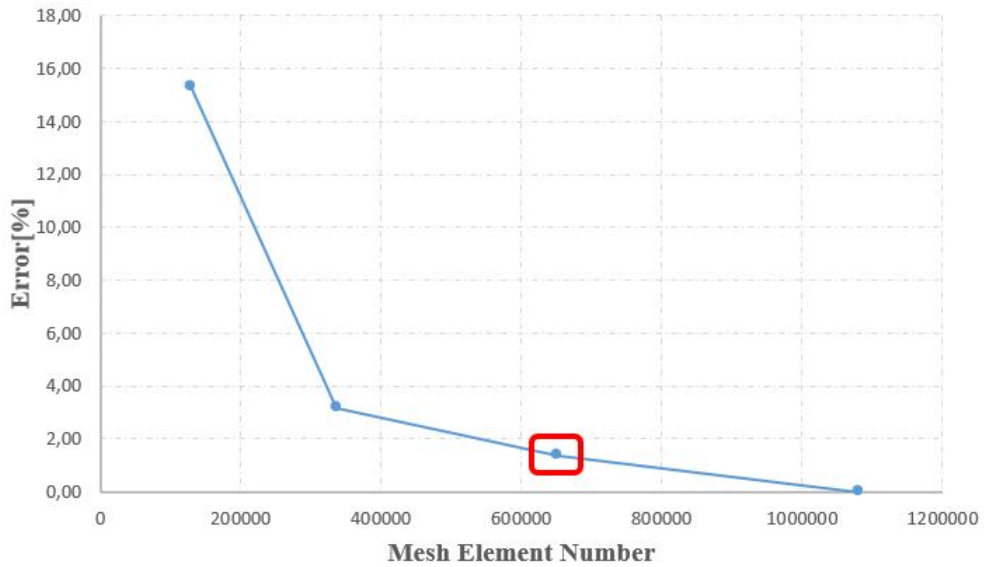


Figure 4.6: Mesh Independency Graph

Table 4.4: Physical Properties of the Multi-Phase Flow at 20°C

Property	Value	Unit
Saturation Pressure	2300	Pa
Water Density	998	kg/m^3
Kinematic Viscosity of Water	9×10^{-7}	m^2/s
Vapor Density	0.02308	kg/m^3
Kinematic Viscosity of Vapor	4.273×10^{-4}	m^2/s
Surface Tension	0.07	N/m

4.3.4 Solver

The *interPhaseChangeFoam* solver is chosen to solve multi-phase flow through the cavitating Venturi. It uses PIMPLE algorithm. k-omega SST turbulence model is applied. The time step is adjusted according to maximum Courant Number specified in the “system” file.

In Figure 4.7, transient mass flow results using three different time steps are compared. In this graph, the oscillation period, which is one of the key characteristic of the cavitation mechanism, is examined. The results are shared in Table 4.5. There is

no difference between the frequency results with CFL number 1 and 0.2. From this point on, all analyzes will be conducted by using a maximum CFL number of 1 due to the computational cost.

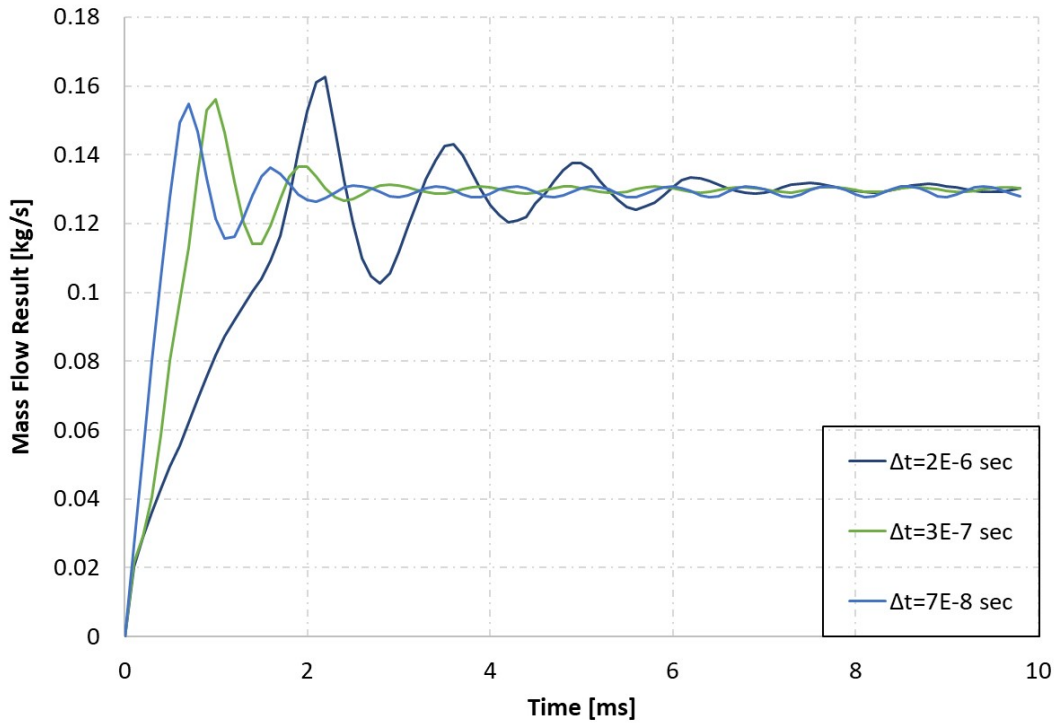


Figure 4.7: Time Step Independency Graph

Table 4.5: Time Step Independency

$\Delta t[s]$	Maximum CFL Number	Period[ms]
7e-8	0.2	0.95
3e-7	1	0.95
2e-6	5	1.45

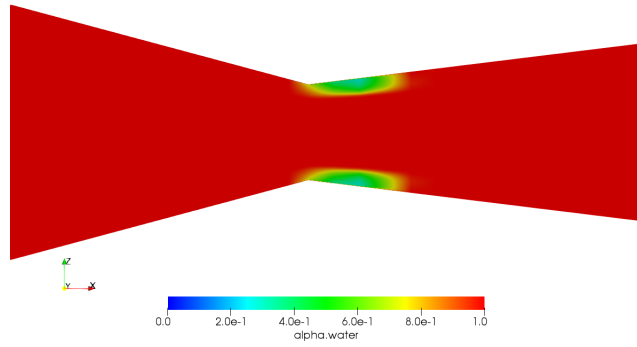
As a cavitation model, available Schnerr-Sauer model is applied. In this model, there is a parameter which is called number density. It is related with the microscopic voids of a bulk fluid which is called nuclei. In principle, this property can be determined via microscopic evaluation of the fluid itself. Microparticles serve as nucleation sites, and it is widely known that "clean" fluids can tolerate and exhibit lower cavitation

threshold pressures as a result of a limited number of sites. Unfortunately, it is very difficult to measure submicron sites that can actively support cavitation, and the influence of the wall (its structure and microchemistry) is also difficult to assess[9]. For this reason, in this study, the sensitivity of results to this parameter is investigated.

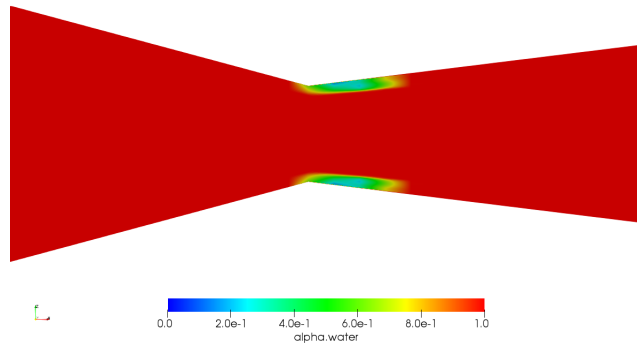
As the number density increases, the cavitation zone is getting rather dense and small. Since the the nuclei number in a cell is increasing, more bubbles are growing and, as a result, vapor to liquid ratio for a cell is increasing.

In Figure 4.9, the velocity contours are compared for different number density values. More bubble generation means more resistant for fluid to flow. Therefore, at maximum number density case, less velocity value has obtained. However, the differences are small.

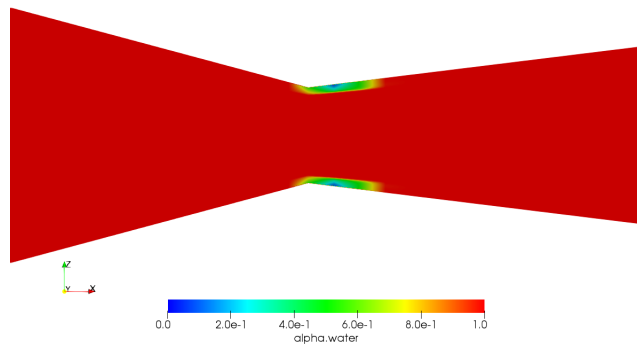
From Figure 4.10, it can be seen that there is no change in the pressure distribution along the centerline of Venturi with respect to different number densities. As a final comparison, the average flow rate values are examined in Figure 4.11. It is concluded that the number density values are not sensitive for the overall results. From this point, all analyzes will be carried out with a number density of $n_0 = 1.6 \times 10^{13}[1/m^3]$.



(a) $n_0 = 1.6 \times 10^{11} [1/m^3]$

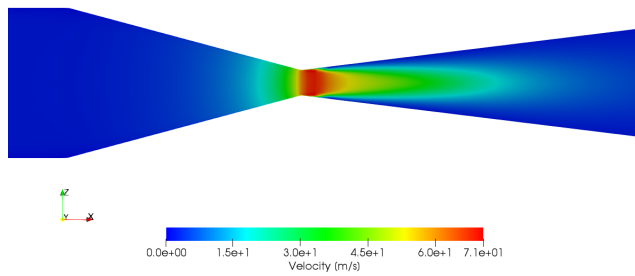


(b) $n_0 = 1.6 \times 10^{13} [1/m^3]$

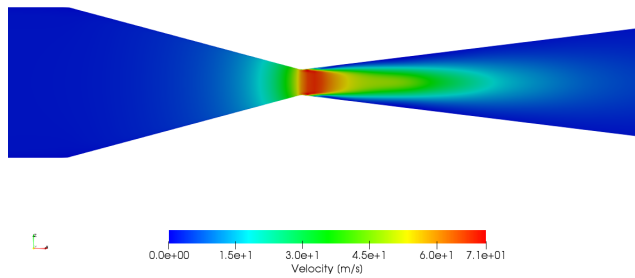


(c) $n_0 = 1.6 \times 10^{15} [1/m^3]$

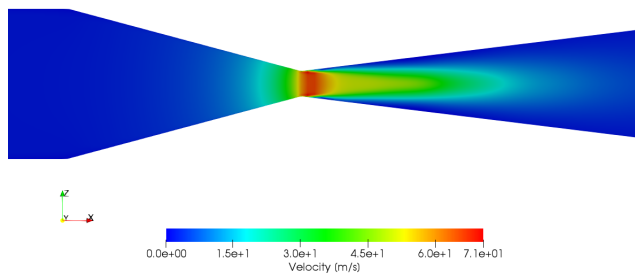
Figure 4.8: Number Density Effect on Liquid Volume Fraction



(a) $n_0 = 1.6 \times 10^{11} [1/m^3]$



(b) $n_0 = 1.6 \times 10^{13} [1/m^3]$



(c) $n_0 = 1.6 \times 10^{15} [1/m^3]$

Figure 4.9: Number Density Effect on the Velocity Magnitude

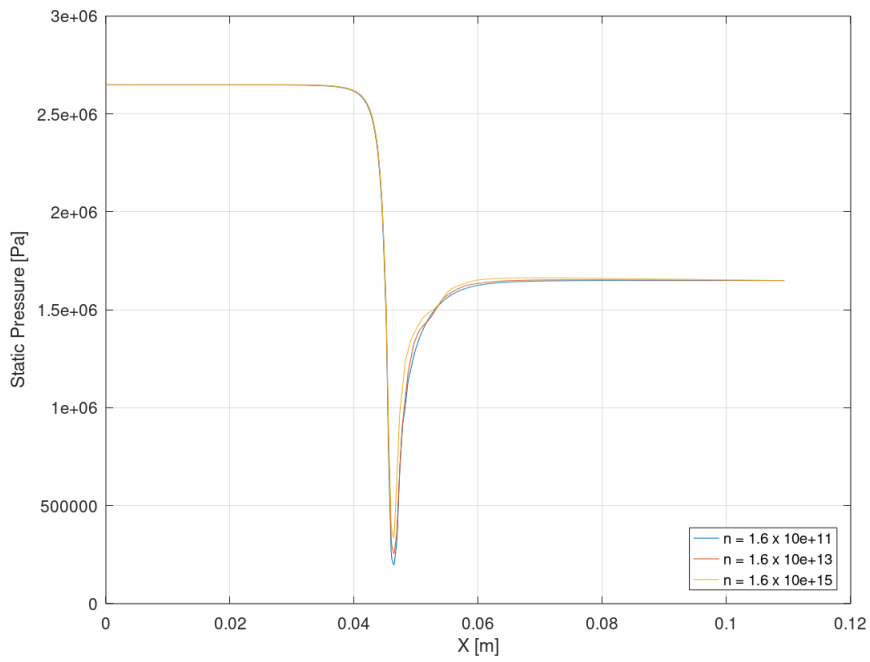


Figure 4.10: Effect of the Number Density on Pressure Distribution along the Center-line of Venturi

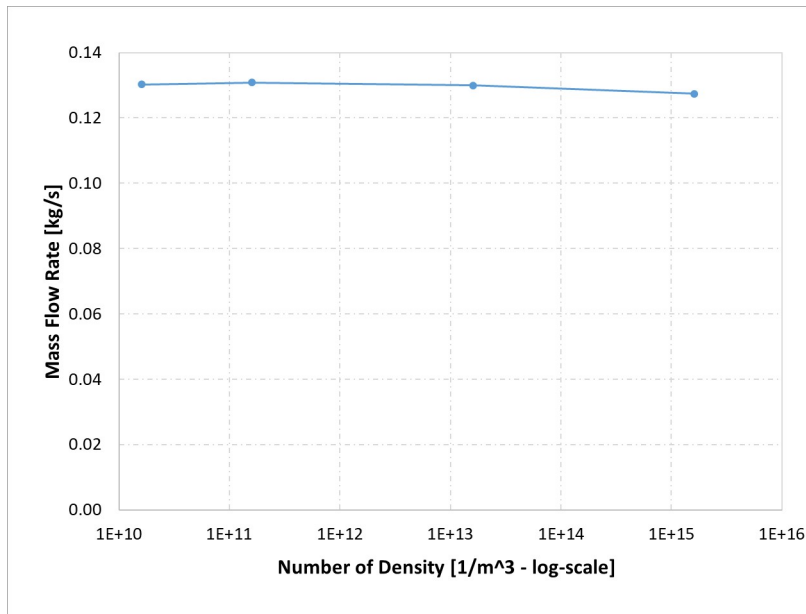


Figure 4.11: Effect of the Number Density on Flow Rate

4.3.5 CFD Result

A bunch of analyzes have been carried out in order to validate the available cavitation model and OpenFoam multi-phase solver. In this section, the transient 3D CFD analyzes related to the cavitating flow are demonstrated and discussed. First of all, cavitation mechanism is investigated as a function of time. Then, the effect of the downstream pressure on the flow rate and cavitation mechanism are examined. In addition, the influence of the upstream pressure on flow is investigated.

4.3.5.1 Cavitation Mechanism Investigation

It can be seen from Figure 4.12, the cavitation starts at the throat and extends up to a certain location of the divergent section. Also, at the same region, wake phenomena which placed just behind the throat due to flow separation can be seen from Figure 4.20. These situations are closely related and the interaction of these two phenomena causes highly unsteady flow.

In the wake zone, high energy loss occurs because of highly turbulent flow. This results in low pressure region after the throat. When the pressure is lower than the vapor pressure of the fluid at the certain temperature, the cavitation occurs (see Figure 4.16). In addition, it can be seen from Figure 4.18, the higher dissipation rate occurs at the near wall. This causes the existing of cavitation at the near wall. On the other hand, at the middle part of the flow area, there is no enough pressure loss in order to see cavitation phenomena.

In Figure 4.19, liquid volume fraction is tracked with time. Bubbles occur at time zero and, they grow and move in the flow direction. At some point, they began to collapse. This collapse results in dividing the cavitation sheet in two pieces. Finally, they disappear at any instant. This process is repeated in the same way.

In Figure 4.20, the flow is investigated by visualizing streamlines. It can be seen that after throat section of the Venturi, the flow separation occurs. This creates low pressure zones near the wall. The bubble formation has occurred at this zone because the local pressure is lower than the vapor pressure of fluid. At the end of the cavitation

zone, circulation occurs.

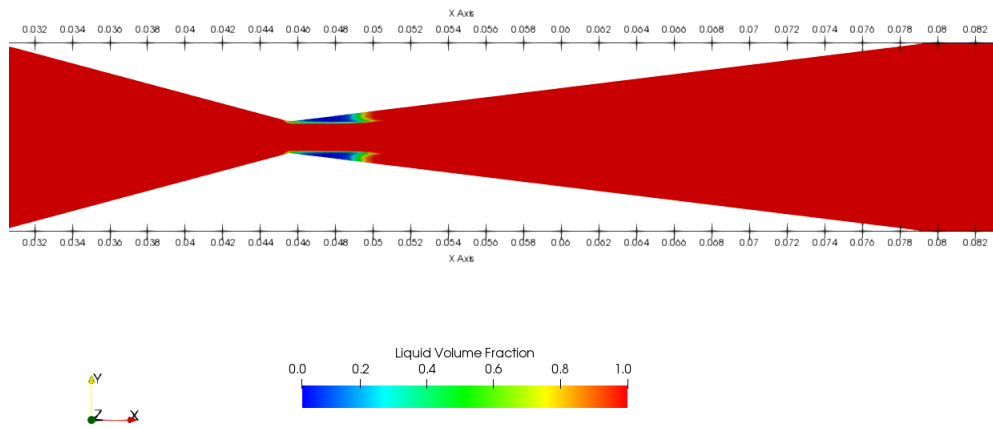


Figure 4.12: Liquid Volume Fraction at $t = 5.1$ ms

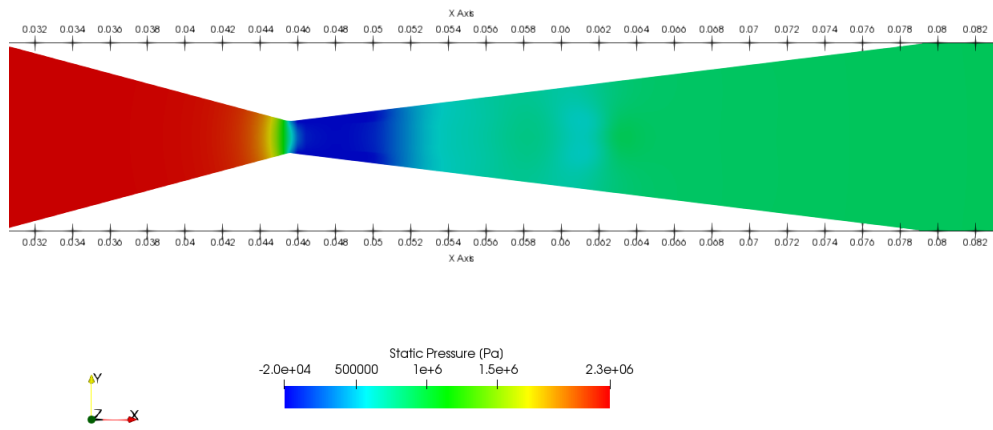


Figure 4.13: Static Pressure at 5.1 ms

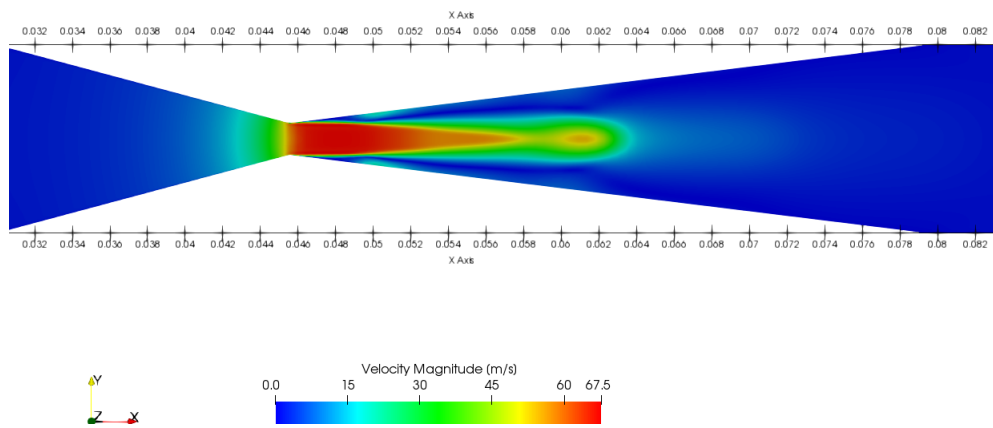


Figure 4.14: Velocity Contour at $t = 5.1$ ms

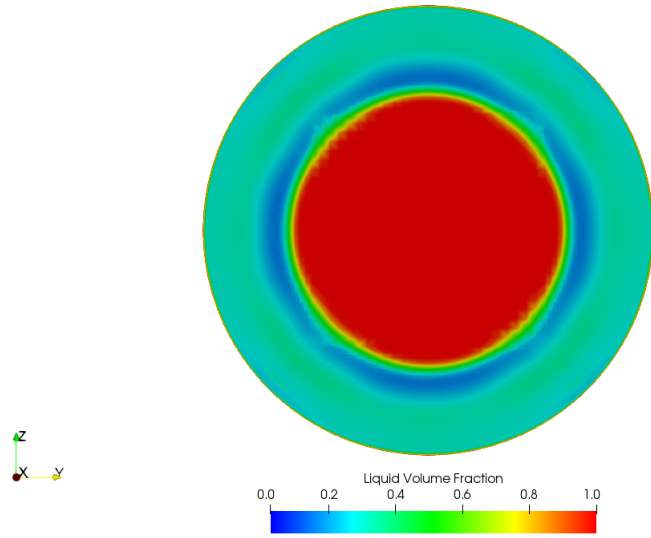


Figure 4.15: Liquid Volume Fraction at yz plane at t = 5.1 ms

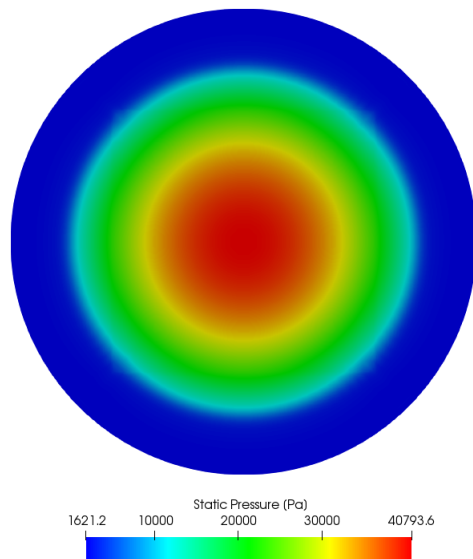


Figure 4.16: Static Pressure at yz plane at t = 5.1 ms

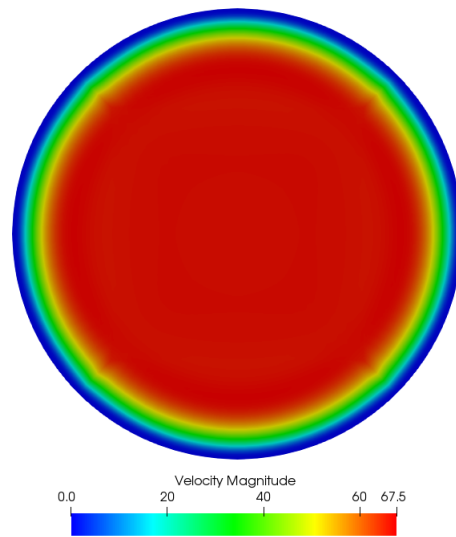


Figure 4.17: Velocity at yz plane t = 5.1 ms

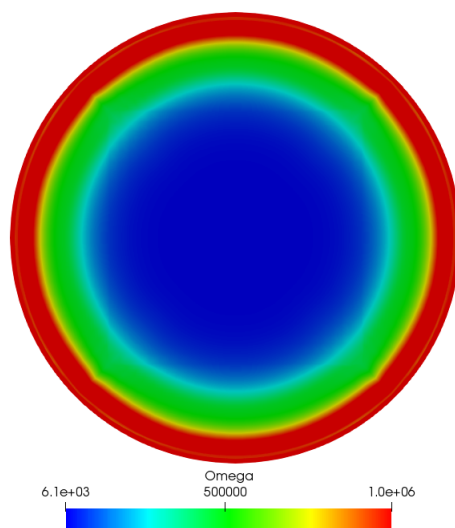
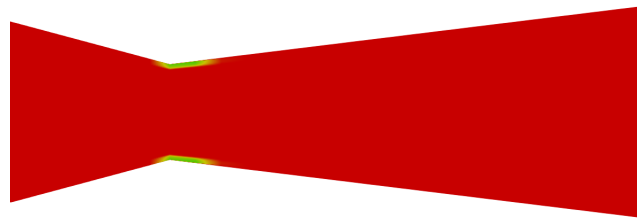
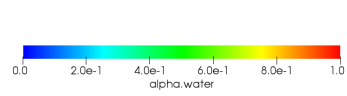
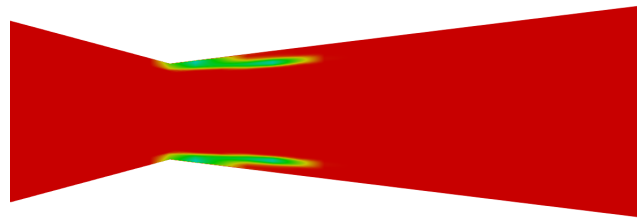


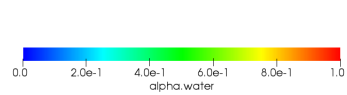
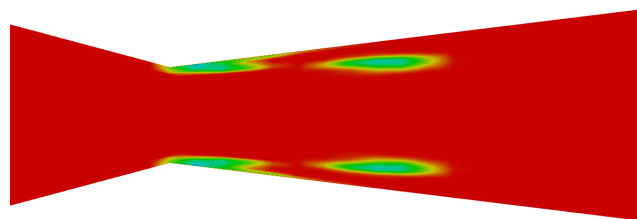
Figure 4.18: Liquid Volume Fraction at yz plane at t = 5.1 ms



(a) $t = 0$ ms

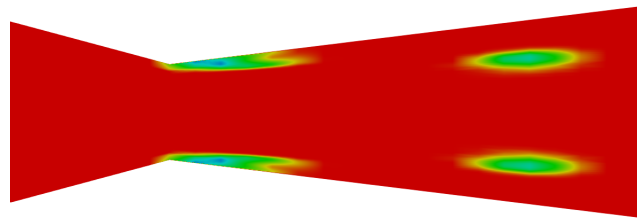


(b) $t = 0.1$ ms

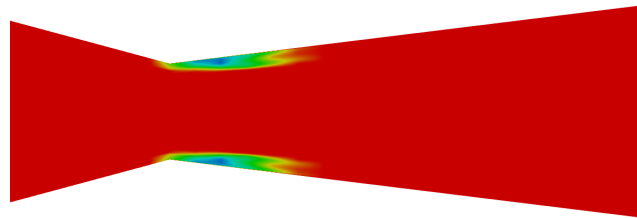


(c) $t = 0.2$ ms

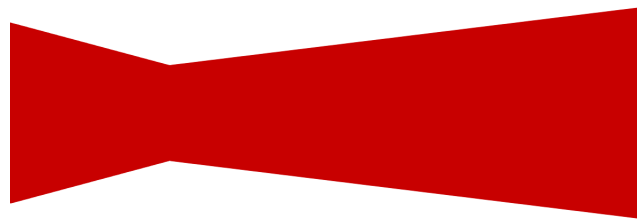
Figure 4.19: Liquid Volume Fraction vs. Time



(d) $t = 0.3$ ms



(e) $t = 0.4$ ms



(f) $t = 0.5$ ms

Figure 4.19: Liquid Volume Fraction vs. Time

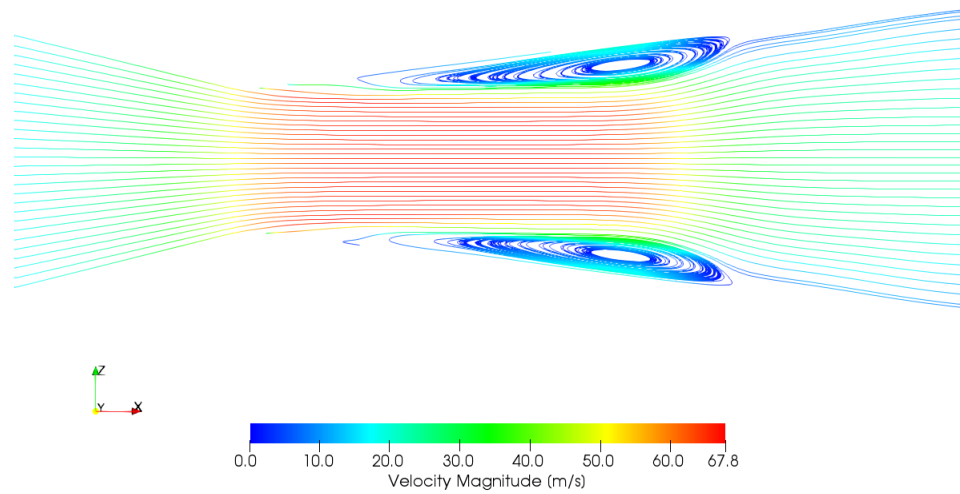


Figure 4.20: Typical Streamlines inside the Venturi

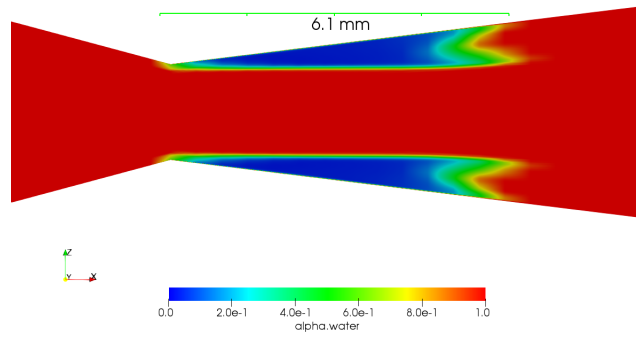
4.3.5.2 Effect of the Downstream Pressure on the Cavitating Flow

In this section, the downstream pressure has been varied to observe effects on the flow. In the CFD analysis, the inlet pressure of the Venturi is kept constant.

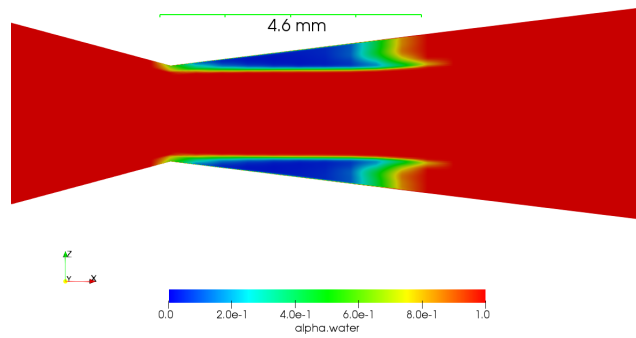
It can be observed from Figure 4.21, when the downstream pressure is decreasing, the cavitation length is increasing at the same inlet pressure. The bubbles propagate more to the Venturi outlet. In the literature, this phenomenon is also studied and it is stated that there is a relation between cavitation length and cavitation number which is proportional to the inlet/outlet pressure ratio[9].

On the other hand, when we look at the effect of the downstream pressure on the mass flow rate through the Venturi, the average mass flows are very close to each other. However, the oscillation frequency is changing with the downstream pressure. In the Figure 4.22, this comparison can be found.

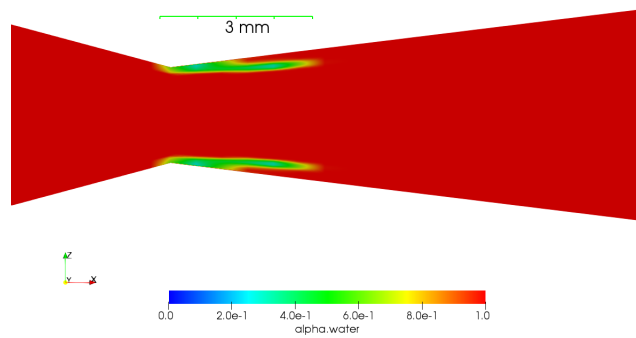
The flow oscillations are strongly dependent on the inlet/outlet pressure ratio. However, the average mass flow rates are not changing. This indicates that the flow rate is independent of the downstream pressure. The results are tabulated in Table 4.6.



(a) Outlet Pressure 8 bara



(b) Outlet Pressure 10 bara



(c) Outlet Pressure 12 bara

Figure 4.21: Effect of the Downstream Pressure on the Cavitation Length

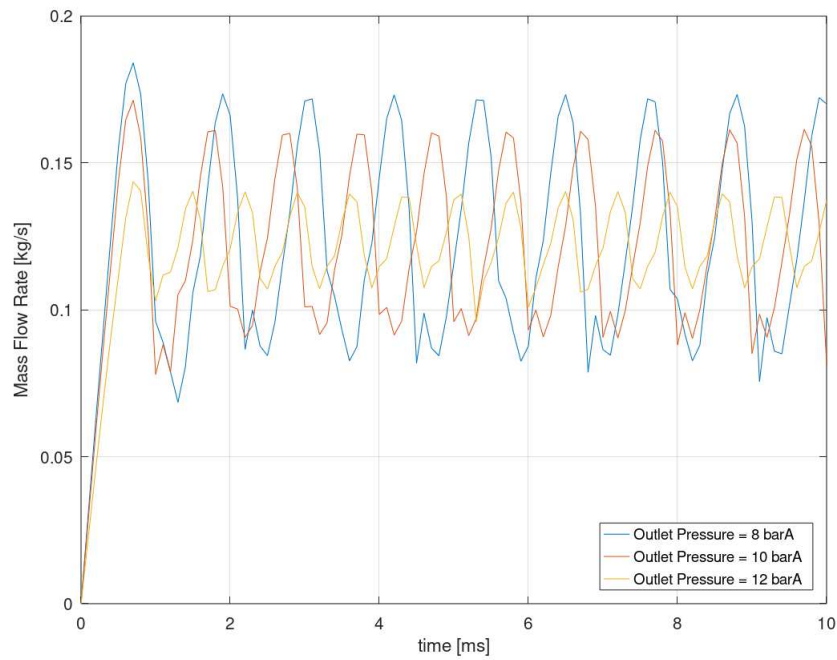


Figure 4.22: Effect of the Downstream Pressure on Flow Oscillations

Table 4.6: The CFD Results

Case	Outlet Press.[barA]	Frequency[Hz]	Avg.Mass Flow Rate[kg/s]
1	8	780	124
2	10	1000	123.9
3	12	1110	123.87

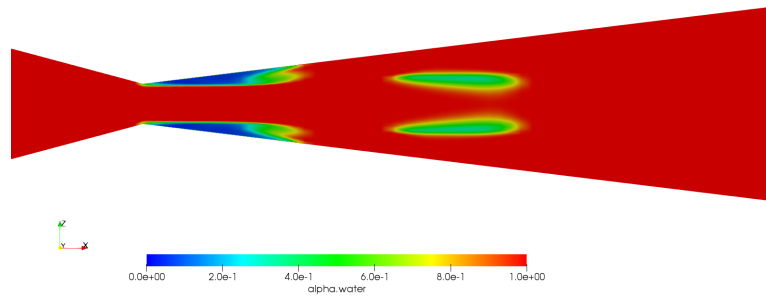
4.3.5.3 Effect of the Upstream Pressure on the Cavitating Flow

The Venturi is analyzed with three different upstream pressure values in this section. The downstream pressure is kept constant for all cases.

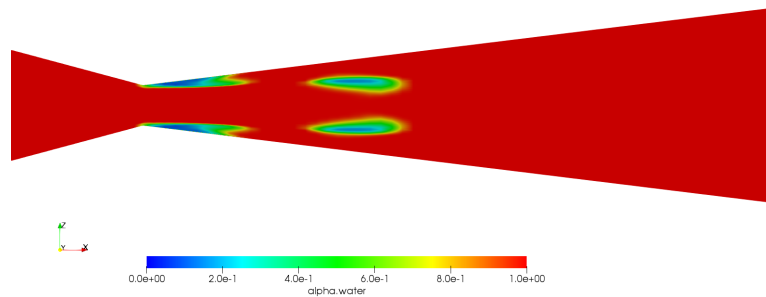
From the Figure 4.23, it can be observed that longer cavitation lengths can be obtained while increasing the upstream pressure. The velocity magnitudes at the throat are directly related to the upstream pressure. Higher velocity magnitude generates more bubbles from the nuclei.

In addition, the mass flow rates through the Venturi are affected by the upstream pressure. There is a comparison of different upstream pressure values to the mass flow rates in Figure 5.3.

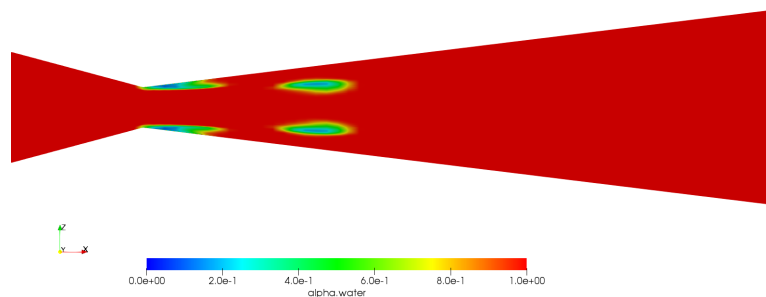
The average mass flow rate is increasing with the increasing of the inlet pressure. Also, the oscillation frequency is affected by the upstream pressure. All results are presented in Table 4.7.



(a) Inlet Pressure at 26 bara



(b) Inlet Pressure at 23 bara



(c) Inlet Pressure at 20 bara

Figure 4.23: Effect of the Upstream Pressure on the Cavitation Length

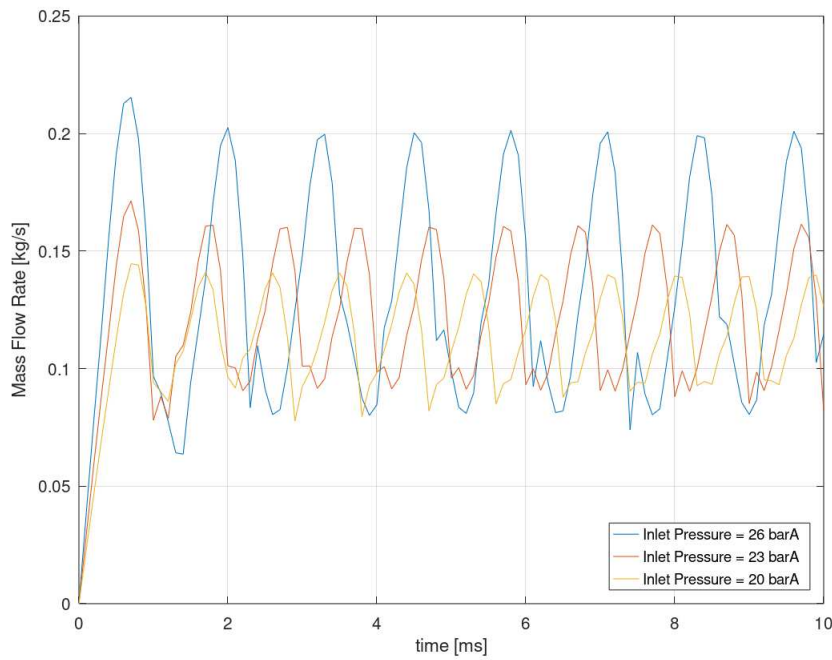


Figure 4.24: Mass Flow Comparison for Different Upstream Pressure Values

Table 4.7: The CFD Results

Case	Inlet Pressure[barA]	Mass Flow Rate[kg/s]
1	20	0.116
2	23	0.123
3	26	0.140

4.4 Variable Area Cavitating Venturi Case

After completing the validation, a numerical study is carried out for a variable area cavitating Venturi. 3D transient CFD simulation has been conducted by using OpenFOAM software. The same solver and model types are used as in the validation case. The only differences are the geometry and domain.

Mesh and time independence studies are not done for this part again. The “*interPhaseChangeFoam*” solver is used during the analyzes. *k-omega* SST turbulence

model and Schnerr-Sauer cavitation model are also applied again.

4.4.1 The Geometry and Boundaries

It is desired to have a variable area Venturi, which enables to regulate the flow for the certain range of the same inlet pressure. Also, it should work in the cavitating regime in order to create an isolation between inlet and outlet. The maximum mass flow rate is intended to be at a certain level. Finally, the inlet and outlet pipe diameters should be 10 mm.

In order to satisfy the requirements mentioned above, the preliminary Venturi design has been carried out with the help of analytical methods which is presented in Chapter 2. In this design, there is a pintle mechanism which can move back and forth. With the help of this mechanism, the flow area can be adjusted in a desired way.

The design parameter is presented in Table 4.8.

Table 4.8: The Design Parameters of the Variable Area Venturi

Inlet Diameter	10 [mm]
Outlet Diameter	10[mm]
Throat Diameter	4.5 [mm]
Pintle Diameter	5 [mm]
Pintle Angle	5 degree

The mesh has been created in the Salome software. Also, the boundary faces are designated as inlet, outlet and wall. The element size is the same as in the validation case which is around 600 000.

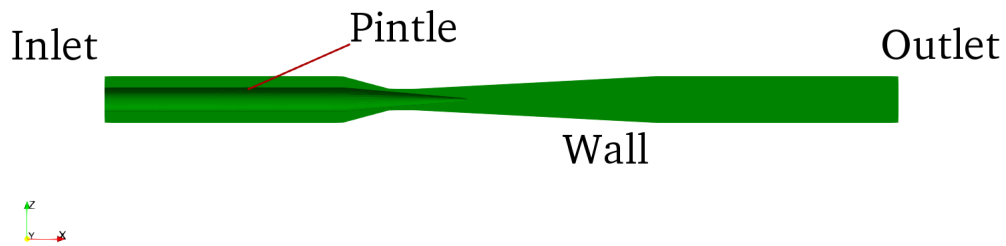


Figure 4.25: The Geometry and Boundary Faces

In this case, y plus criteria has been checked between inlet and outlet of the geometry. Y plus can be kept approximately in the range of 30 to 50. Since the wall function is used y plus can be greater than a certain value and coarser mesh can be applied to reduce computational time.

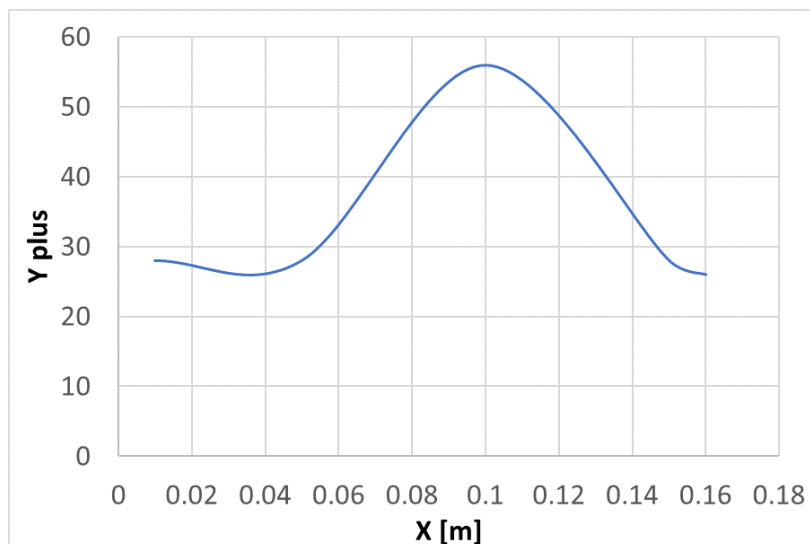


Figure 4.26: Y-plus for Variable Area Venturi

4.4.2 CFD Results

In this section, CFD simulations of the variable area cavitating Venturi are presented. The analyzes are carried out for different pintle strokes and downstream and upstream pressures. The time-dependent analyzes are performed with satisfying maximum CFL number of 1.

4.4.2.1 Different Pintle Strokes

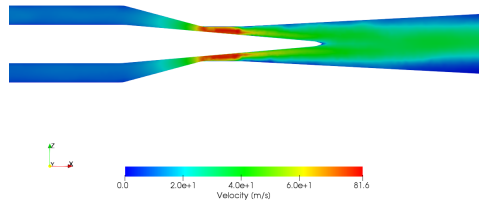
In order to see variation of the flow rates through the variable area cavitating Venturi with the different pintle stroke values, five different case file has been created. The main aim is to examine the flow rates corresponding to the different stroke values and cavitation phenomena.

The reference point is the contact point between the pintle and the throat. While increasing the stroke, the flow area is also increasing.

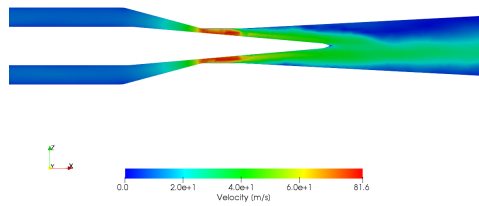
In Figure 4.27, the velocity profiles can be seen. The highest velocity magnitudes are observed in the narrow section as expected. From the transient simulations, it can be seen that the pressure and velocity profiles are highly unsteady. However, the vapor to liquid ratio is not oscillating as much as in the validation case. In this case, the bubbles occur at the highest velocity zones.

In Figure 4.29, it can be observed that for the first three cases, the cavitation length does not change. However, the cavitation length is smaller than the others for the last case, since there is a higher pressure loss before throat region.

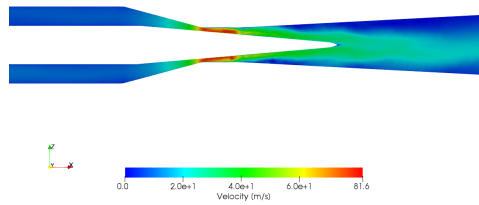
In Figure 4.30, it is clearly seen that as the stroke increases, the mass flow also increases.



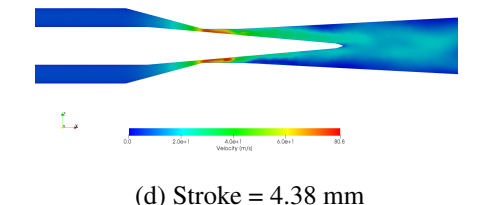
(a) Stroke = 7.38 mm



(b) Stroke = 6.38 mm

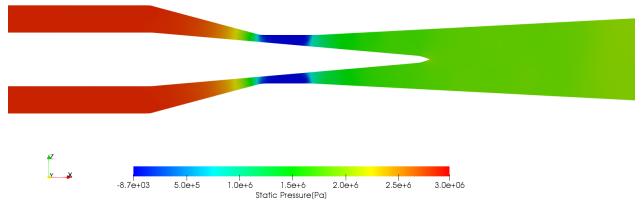


(c) Stroke = 5.38 mm

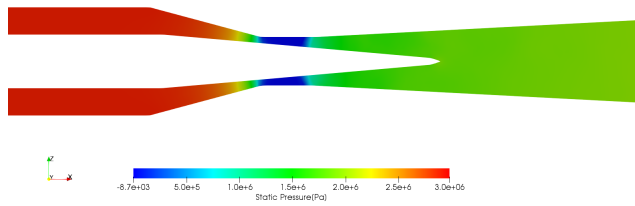


(d) Stroke = 4.38 mm

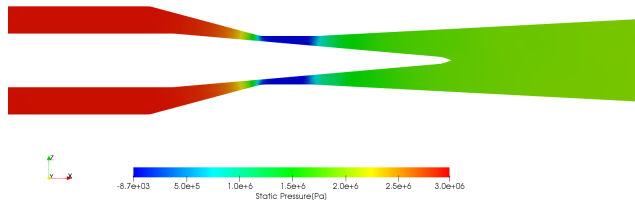
Figure 4.27: Velocity Contours for Different Stroke Values



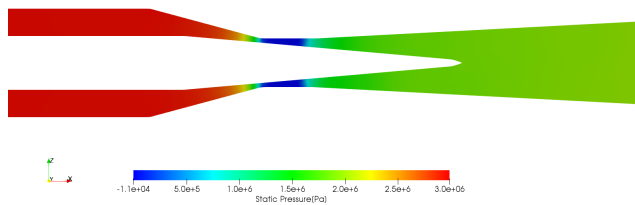
(a) Stroke = 7.38 mm



(b) Stroke = 6.38 mm

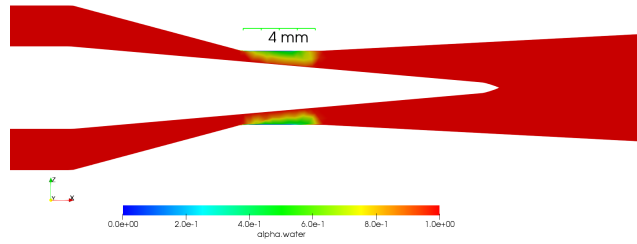


(c) Stroke = 5.38 mm

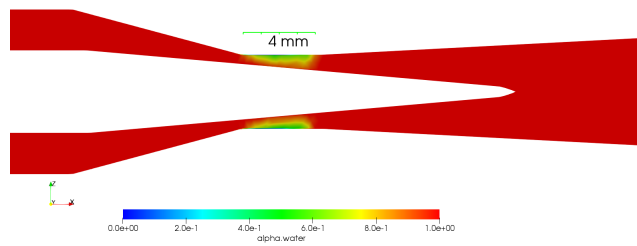


(d) Stroke = 4.38 mm

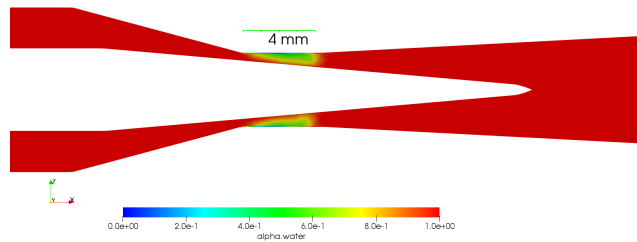
Figure 4.28: Pressure Contours for Different Stroke Values



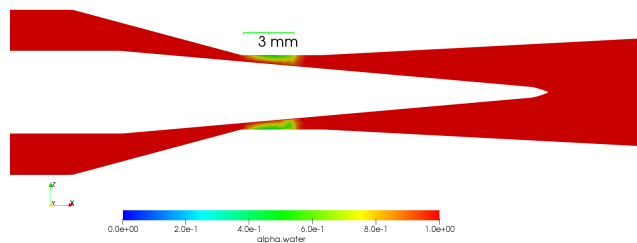
(a) Stroke = 7.38 mm



(b) Stroke = 6.38 mm



(c) Stroke = 5.38 mm



(d) Stroke = 4.38 mm

Figure 4.29: Liquid Volume Fraction for Different Stroke Values

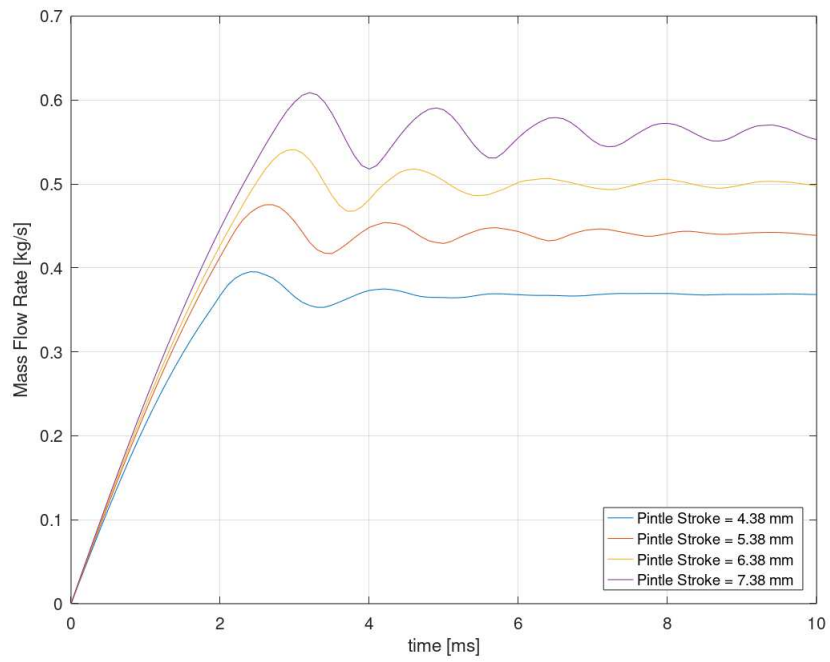
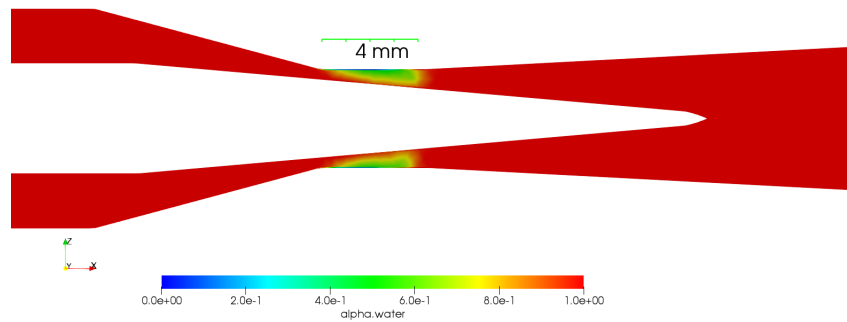


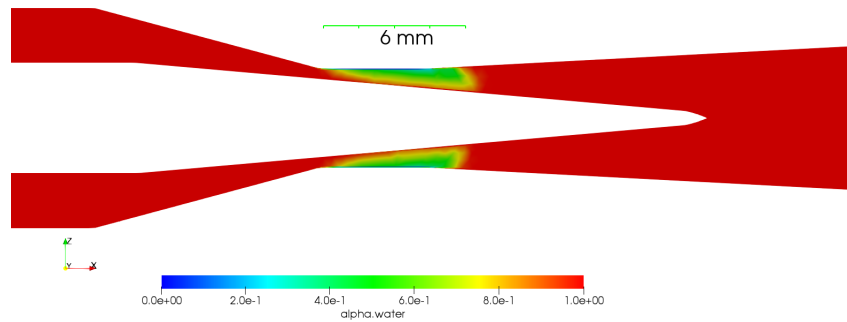
Figure 4.30: Mass Flow Rates for Different Stroke Values

4.4.2.2 Effect of Downstream Pressure

Two different downstream pressure values are selected on the flow. Their effect on the cavitation length has been examined in Figure 4.31.



(a) Outlet Pressure 20 bara



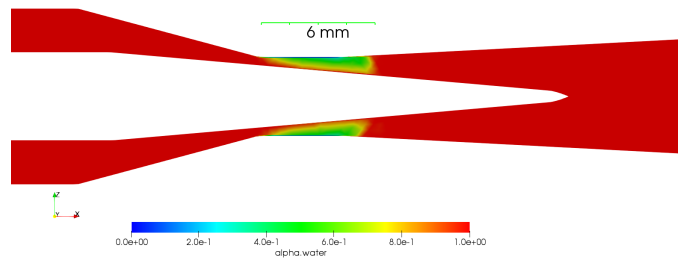
(b) Outlet Pressure 15 bara

Figure 4.31: Effect of the Downstream Pressure on the Cavitation Length

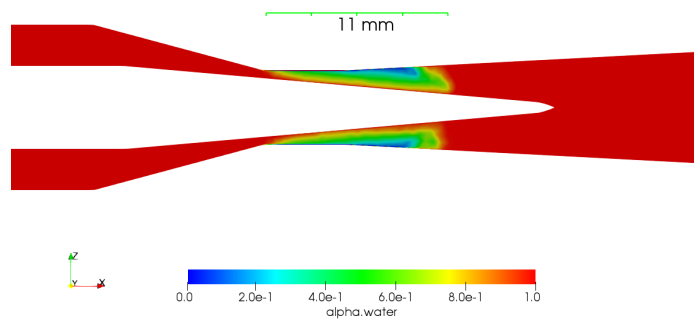
4.4.2.3 Effect of Upstream Pressure

The mass flow rate is dependent of the inlet pressure in the Venturi. Therefore, it is very critical to see the characteristics of the Venturi at different inlet pressures.

In Figure 4.32, it appears that the larger inlet pressure increases the cavitation length at the same outlet pressure.



(a) Inlet Pressure 40 bara



(b) Inlet Pressure 50 bara

Figure 4.32: Effect of the Inlet Pressure on the Cavitation Length

CHAPTER 5

RESULTS AND DISCUSSIONS

In this chapter, all experimental and numerical studies are examined together. All results are summarized.

In the numerical studies, a time dependent and 3D CFD simulations of the fixed area cavitating Venturi have been carried out as a validation case. Then, the variable area cavitating Venturi analyzes have been conducted by using OpenFoam software. All models and solver types are the same as the ones in the validation case.

It is very important to compare the simulation results and test results in such a consisting multi-physics case. To do this, a fixed geometry cavitating Venturi is experimentally examined and all the available experimental and numerical simulation results are compared in this chapter. Considering the time and cost issues, the variable area cavitating Venturi experiments cannot be performed in this study. The simulations of the cavitating flow will be compared by using only experimental results of the fixed area cavitating Venturi. For the variable area cavitating Venturi experiments, more advanced experimental set-up and sensors are needed. However, if the cavitating flow can be validated with the available experiments, the model and CFD simulation parameters can be used for further investigations including variable area cavitating Venturi.

In this chapter, some non-dimensional parameters are used in order to obtain more meaningful conclusions. For this reason, cavitation number and discharge coefficient are defined as follows:

$$\sigma = \frac{P_{inlet} - P_{vapor}}{P_{inlet} - P_{outlet}} \quad (5.1)$$

$$C_d = \frac{\dot{m}_{real}}{\dot{m}_{theoretical}} \quad (5.2)$$

5.1 Comparison of Experimental and Numerical Results

In this section, the fixed area cavitating Venturi simulation and experimental results are compared in terms of mass flow rate and effects of the downstream and upstream pressure on the flow behavior. Since there are so many tests and numerical simulation cases, it is better to give all the case involving the results.

Table 5.1: Test Metrix

Case No	P_{inlet} [bara]	P_{outlet} [bara]	\dot{m} [kg/s]	σ	Cd	Re
1	26	3.2	0.162	1.13	0.93	23×10^3
2	26	1.6	0.162	1.06	0.93	23×10^3
3	26	7.4	0.162	1.35	0.93	23×10^3
4	24.8	4	0.153	1.19	0.88	22×10^3
5	24.2	3.8	0.153	1.185	0.88	22×10^3
6	23.9	3.9	0.152	1.19	0.90	21.5×10^3
7	23.4	11.7	0.152	2	0.92	21.5×10^3
8	23.2	7.6	0.151	1.48	0.92	21.5×10^3
9	23.1	5.8	0.149	1.33	0.90	21.5×10^3
10	22.5	5.2	0.147	1.3	0.91	21×10^3
11	22.1	11.2	0.146	2.02	0.91	21×10^3
12	20.9	9.7	0.138	1.86	0.82	18×10^3
13	17.6	1.2	0.121	1.07	0.84	17×10^3
14	23-20	Variable	-	-	-	-

As it can be seen from the Table 5.1, the fixed area Venturi has been tested at different conditions. Some tests have been conducted more than once in order to check repeatability. This matrix may differ from the test matrix which is presented in Chapter 3. As it can be seen from the last row of the matrix, the Venturi is tested at dynamic

boundary conditions.

Since the flowmeter which is used in the experimental set-up cannot make a measurement as fast as to sense the flow oscillations, all flow rate data gathered during the test duration is averaged. All mass flow rate results are the average values.

There is also a simulation matrix which is given in the Table 5.2. The mass flow rate data are averaged when the simulations reach quasi-steady situation.

Table 5.2: The Fixed Area Cav.Venturi Simulation Matrix

Case No	P_1 [bara]	P_2 [bara]	Dur.[ms]	\dot{m} [kg/s]	σ	Cd	Re
15	26	10	10	0.140	1.62	0.87	20×10^3
16	23	10	10	0.124	1.76	0.83	17.7×10^3
17	20	10	10	0.116	2	0.83	16.6×10^3
18	23	8	10	0.124	1.53	0.83	17.7×10^3
19	23	12	10	0.124	2.1	0.83	17.7×10^3
20	23	05	10	0.124	1.27	0.83	17.7×10^3

5.1.1 Mass Flow Rate Comparison

During the investigation of Tables 5.1 and 5.2 , the differences in flow rates are remarkable. This difference seems to have increased up to 15 percent (see Figure 5.1).Therefore, the results of the CFD simulations are unacceptable. When this situation was investigated in detail, it was decided to perform dimensional measurements of the tested Venturi. The illustrations related with the dimensional measurement are given in Figure 5.2.

The Venturi throat diameter has been designed to be 1.68 mm. All CFD simulations are done according to this diameter value. However, in reality, the Venturi throat diameter is 1.755 mm due to manufacturing tolerances. It was decided to change the geometry in the CFD analysis since it would take a long time to perform the tests with a remanufactured Venturi.

When looking at Figure 5.3, the difference between test results and CFD results are

below 4% in terms of the mass flow rate. Since the throat diameter is the most dominant parameter for the flow rate, the sensitivity of this parameter is significant.

It can be concluded from the tests and CFD simulations that the mass flow rate remains constant at different downstream pressures. Hence, the flow is independent from the exit pressure.

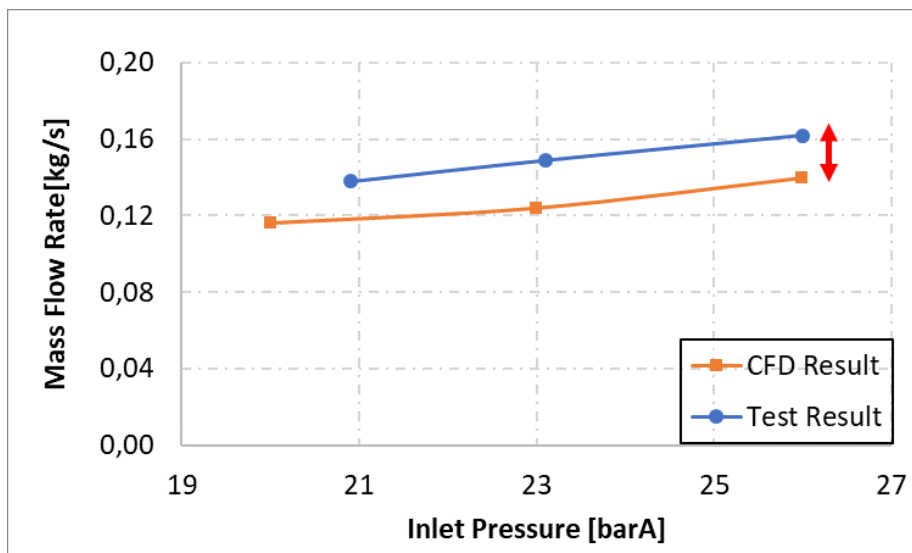
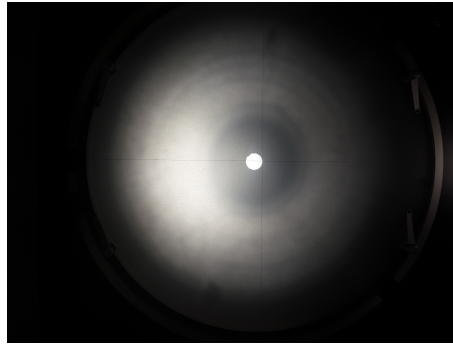
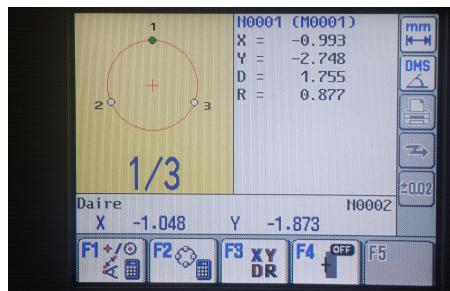


Figure 5.1: Mass Flow Rate Comparison



(a)



(b)

Figure 5.2: The dimensional measurement of the tested Venturi

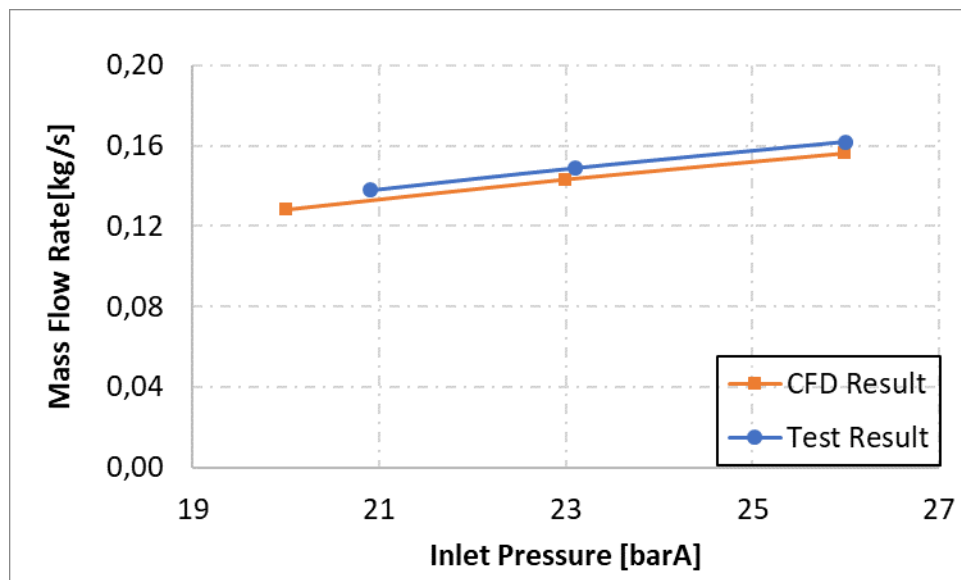


Figure 5.3: Mass Flow Comparison with 1.75 mm Thoroat Diameter Venturi

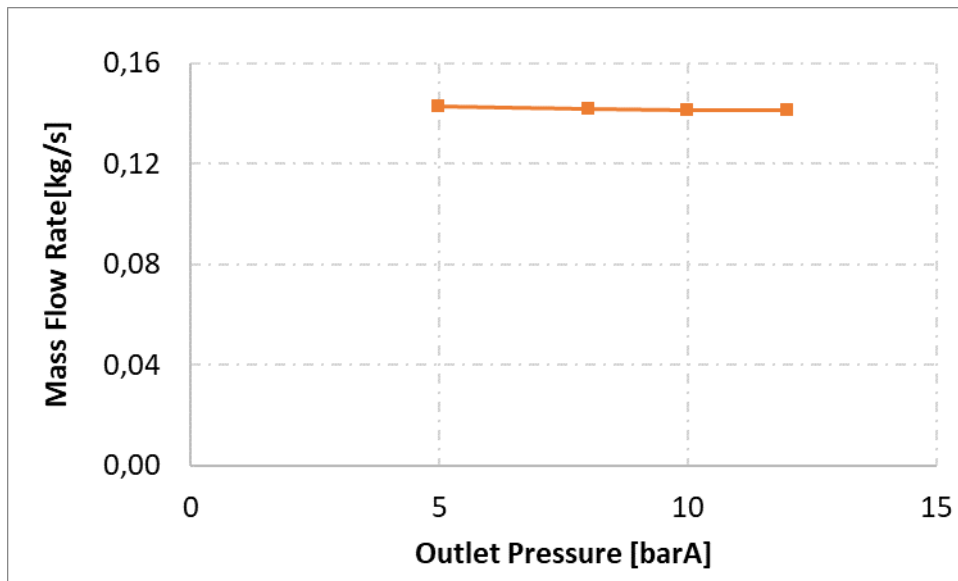


Figure 5.4: Mass Flow Rate vs Downstream Pressure(CFD Simulations) (Pinlet = 23 bara)

5.1.2 Oscillation Frequency

In the previous chapter, the experimental procedure has been explained. In order to see cavitation phenomenon, the flow through the transparent Venturi is observed with the help of high speed camera. In addition, the flow oscillation due to cavitation mechanism has been examined during the transient CFD simulations in Chapter 3. Now, the experimental and numerical studies related with these phenomenon are compared with each other.

In Figures, 5.5 and 5.6, the boundary conditions are similar. The period of the two results does not show good agreement. However, the cavitation split, cavitation cycle are very similar.

There is a relation between flow oscillation and cavitation mechanism which consisting of bubble generation and collapsing. In Figure 5.9, this relation is illustrated.

The oscillation frequency can be observed in three different ways in this study. In addition to CFD simulations and flow visualizations, the pressure sensor data which is located at the exit of the Venturi is examined since the pressure and flow rate are

directly related to each other due to incompressible flow. During the tests, the data is collected from the pressure sensor at a 4 kHz sampling rate. If Fast-Fourier Transform is applied to the data, the dominant frequency can be seen easily.

In Figures 5.10, 5.11 and 5.12, the FFT graphs which belong to several test cases are presented.

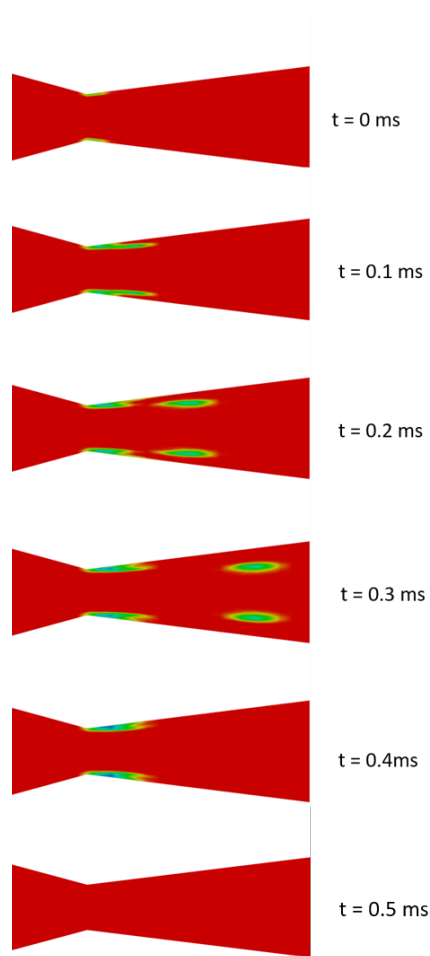


Figure 5.5: The CFD Simulation (Case 19)

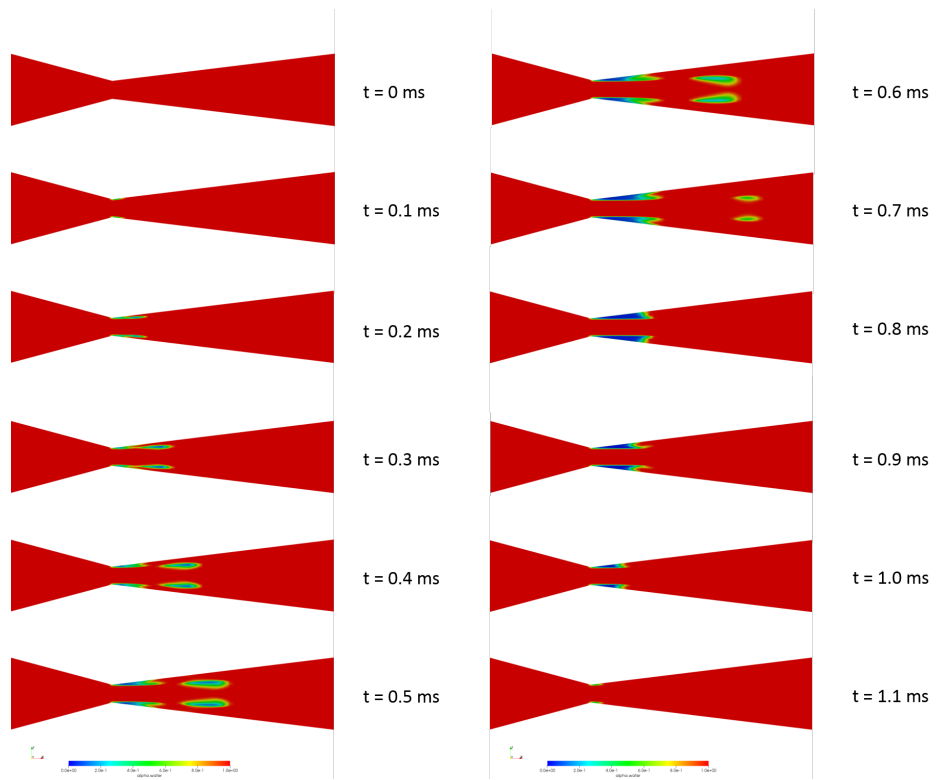
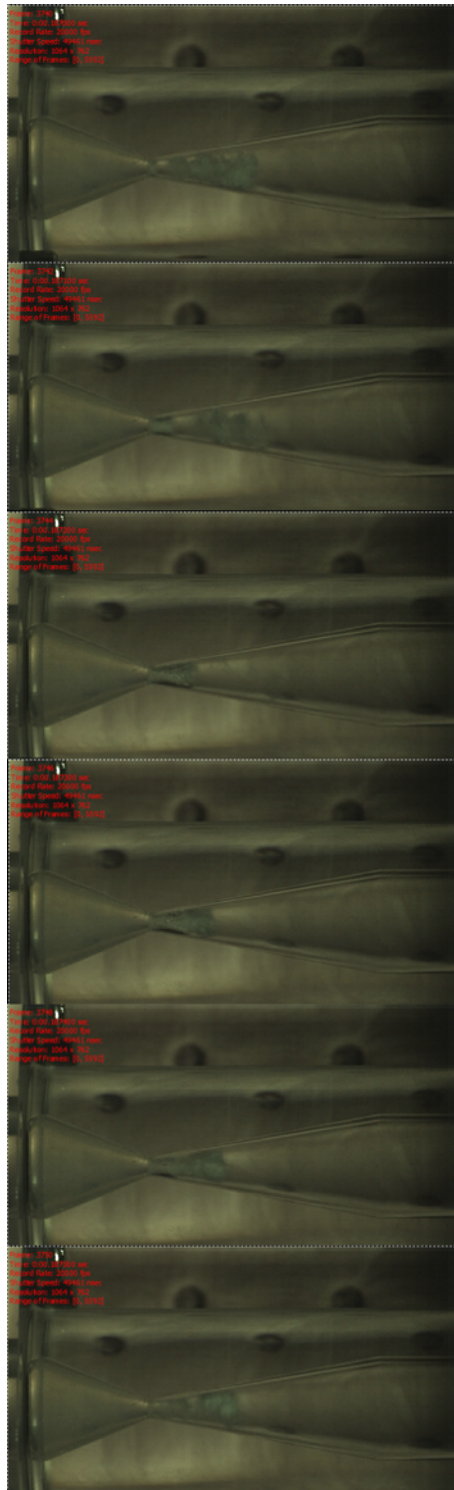


Figure 5.7: The CFD Simulation (Case 16)



t = 0 ms

t = 0.1 ms

t = 0.2 ms

t = 0.3 ms

t = 0.4 ms

t = 0.5 ms

Figure 5.8: The Flow Visualization (Case 8)

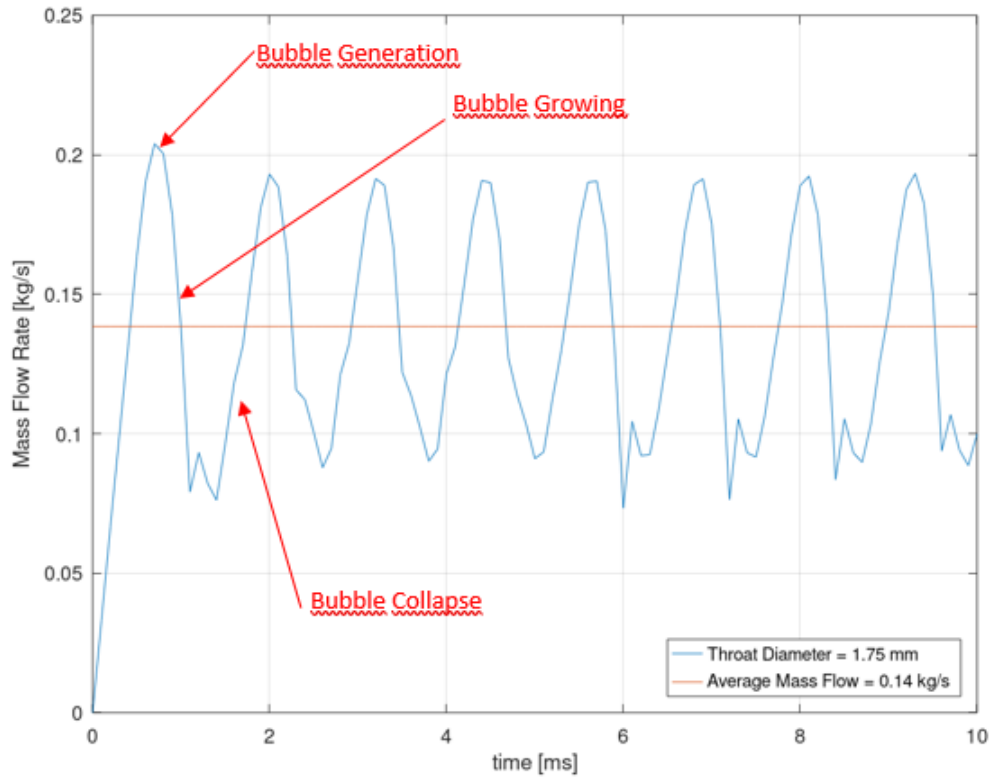


Figure 5.9: Mass Flow Rate vs Time (Case 16)

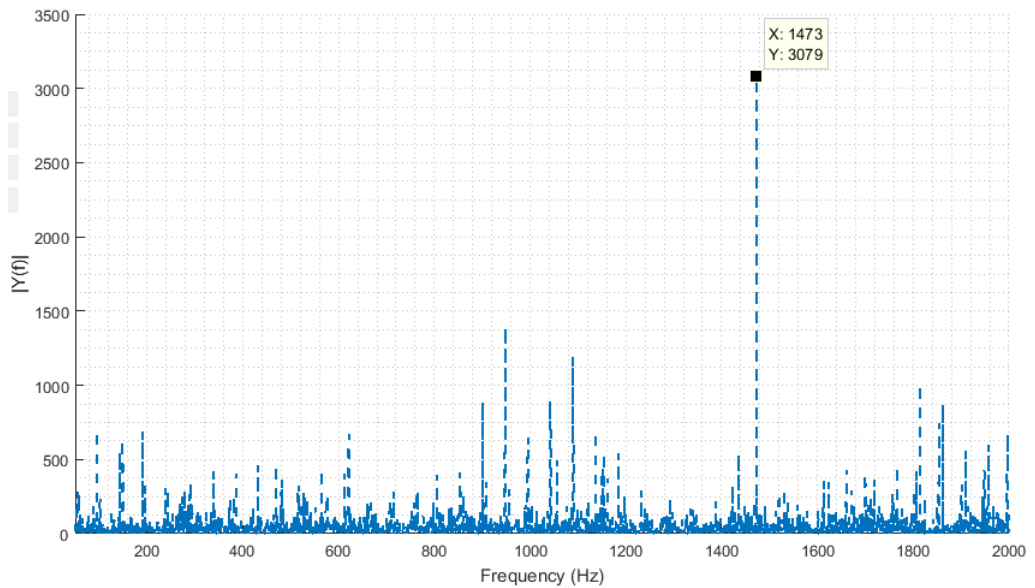


Figure 5.10: FFT of the Pressure Data (Case 7)

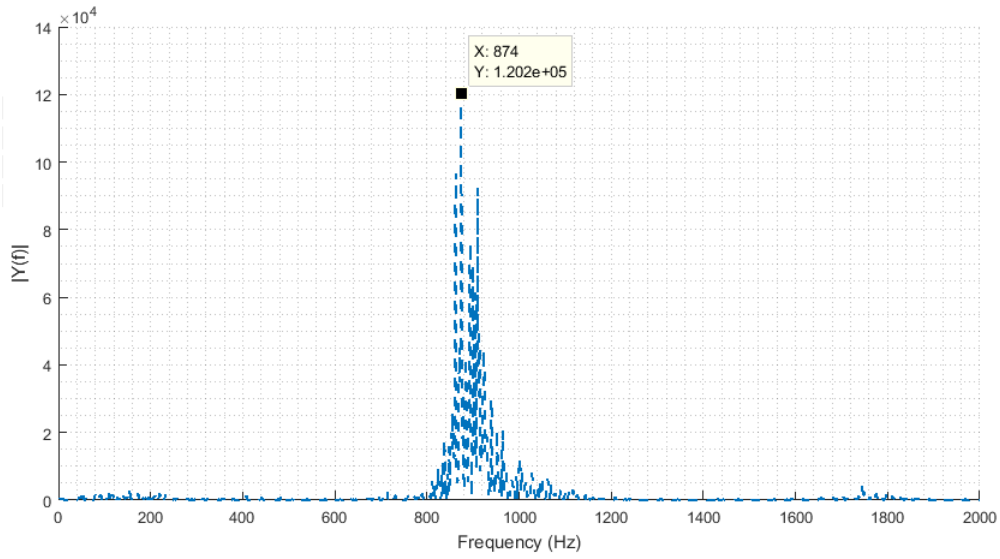


Figure 5.11: FFT of the Pressure Data (Case 9)

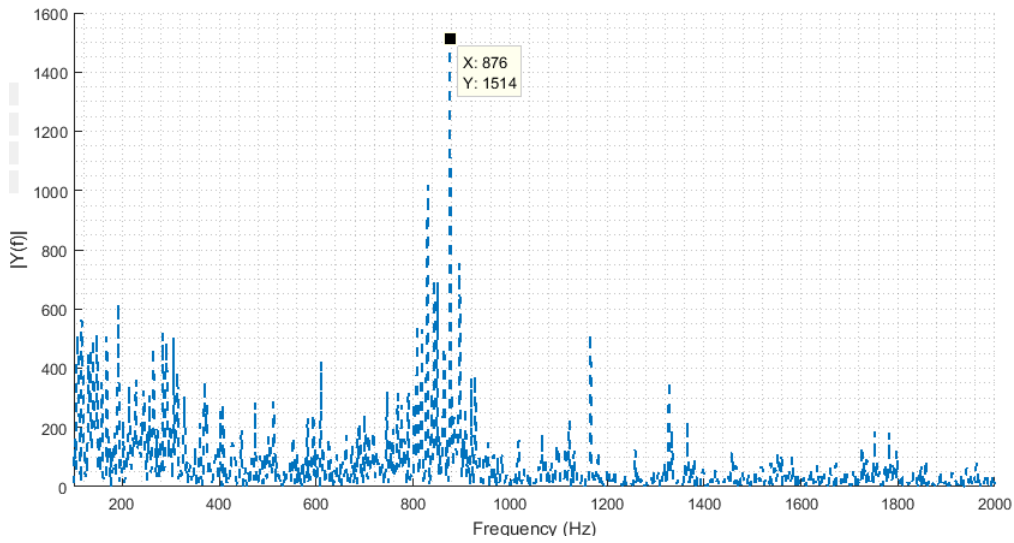


Figure 5.12: FFT of the Pressure Data (Case 10)

All results are presented in the Table 5.3.

Table 5.3: Frequency Results for Related Cases

Case No	σ	CFD	H.S.C.	FFT
7	2	-	2220 Hz	1400 Hz
8	1.48	-	1666 Hz	-
9	1.33	-	-	874 Hz
10	1.3	-	-	876 Hz
16	1.53	780 Hz	-	-
18	1.76	1000 Hz	-	-
19	2.1	1110 Hz	-	-

Since the data acquisition system allow a maximum 4kHz sampling rate, the dominant frequency which is higher than 2kHz cannot be observed by FFT. In Table 5.3, it appears that the oscillation frequency is related to nothing but the cavitation number. As cavitation number decreases, the frequency value increases. However, the amplitude of the oscillations decreases with the increasing frequency. On the other hand, there are some discrepancy between the results although the trend is the same. Since there is a distance between the pressure sensor location and the Venturi exit, the flow conditions may differ for each case.

Also, the simulation results are coherent with the results obtained from the flow visualization. Looking at the overall table, the flow oscillates at high frequency although the amplitude can go up to 20 % of the average mass flow rate. These results are very important for the characterization of the Venturi performance.

5.1.3 Cavitation Length

The cavitation length is another important parameter for the validation of the CFD simulation. In order to make comparison between the test and simulation, the image taken from the high speed camera has been processed using Matlab Image Processor Toolbox. The cavitation length is measured using the pixel coordinate. Since the throat diameter of the Venturi is known, a relation between pixel distance and real

distance can easily be established. In Figure 5.13, the throat diameter is measured as 26 using the pixel coordinate. The total cavitation length is 116. This means that cavitation length is 7.25 mm in real.

During post-processing of the CFD analyzes, the cavitation length is measured as shown in Figure 5.14.

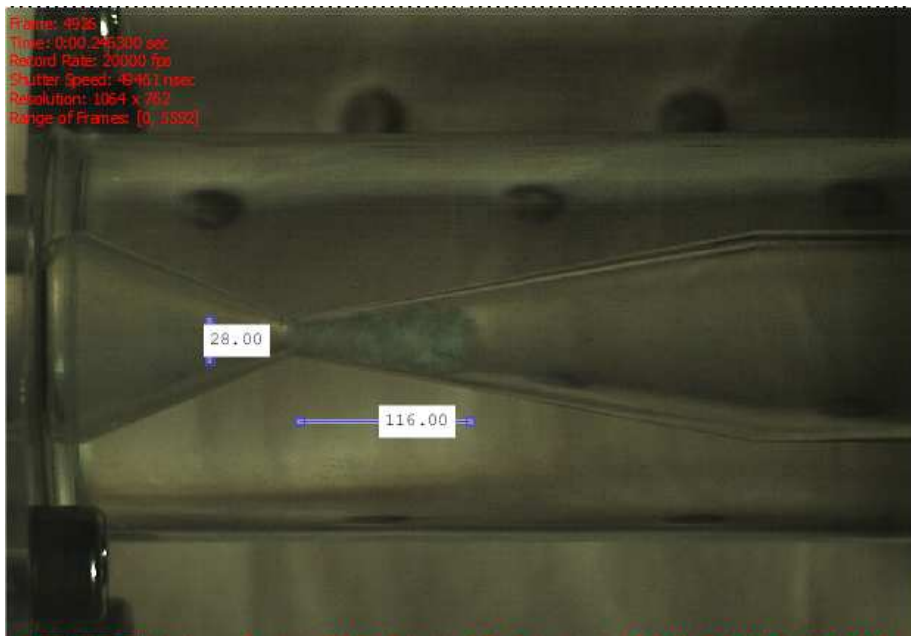


Figure 5.13: H.S.C. Image (Case 8)

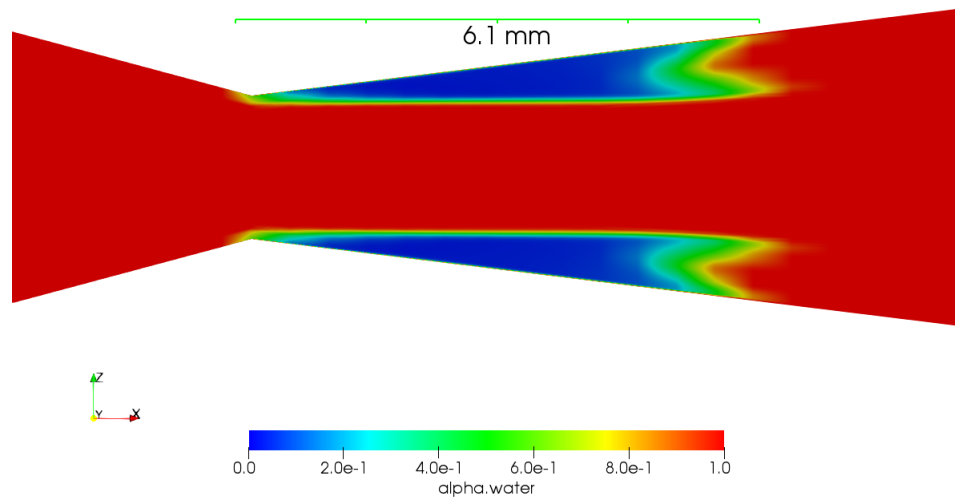


Figure 5.14: CFD Simulation (Case 18)

5.2 Variable Area Cavitating Venturi Case

After all the comparisons related with the test results and simulations are completed, the studies about variable area cavitating Venturi are given in this section. The first design is created with the help of analytical solutions which are mentioned in Chapter 2. In order to determine some critical design parameter, the Tian's study is taken as a reference [8]. In Tian's study, the experimental procedure and results for the variable area cavitating Venturi are presented. At some points, in order to verify the CFD simulations, the results are compared with the Tian's case.

First of all, the main characteristic of the variable area cavitating Venturi is the mass flow rate, which is a function of stroke. The CFD simulations have been carried out at several pintle positions. The flow rate values corresponding to each pintle position is given in the Figure 5.15.

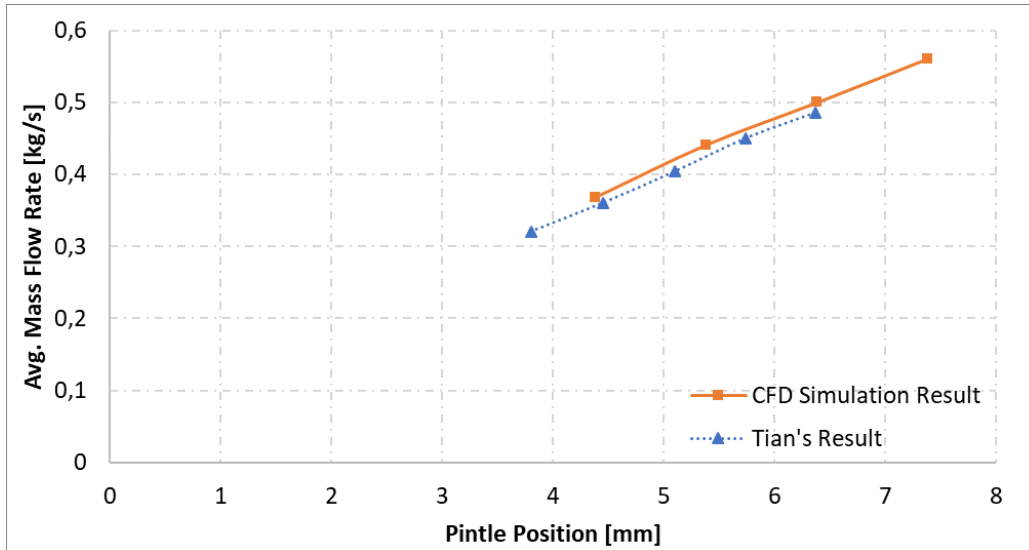


Figure 5.15: Pintle Position vs Flow Rate Graph

As the pintle position is increasing, the flow rate rises linearly due to increasing of the flow area. The linear relation between flow rate and the pintle position is desired for ease controlling for the pintle mechanism. The dimensionless discharge coefficient graph can be seen in Figure 5.16.

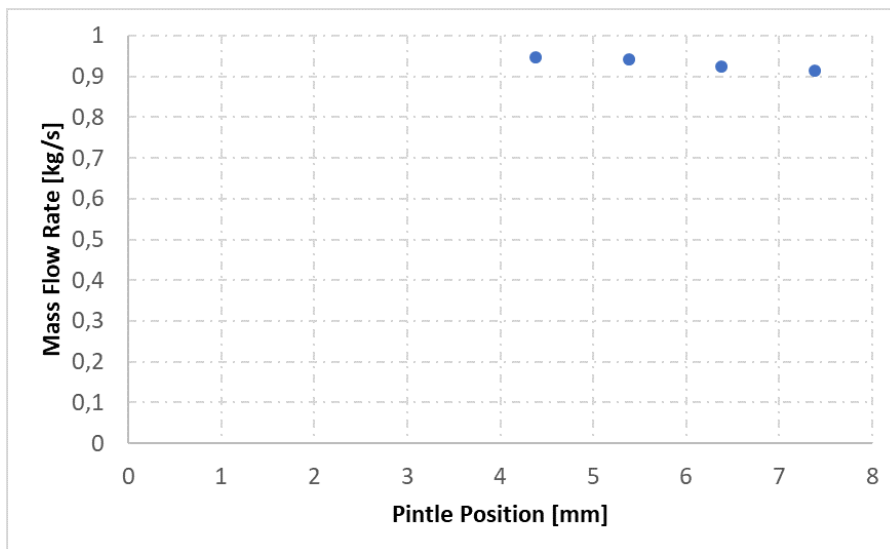


Figure 5.16: Discharge Coefficient Based on CFD Simulations

5.2.1 Outlet Angle of the Venturi Investigation

Since it is not intended to have bubbles at the outlet of the Venturi, there should be a divergent section in the venturi in order to recover the static pressure. Also, it is important to have minimum total pressure loss through the Venturi. Therefore, several CFD simulations have been performed to get optimum outlet angle.

In the table below, the CFD results related with the three different outlet angle are presented. The pintle position is kept constant for all case.

Table 5.4: The Effect of the Outlet Angle

Outlet Angle[deg]	Pintle Stroke [mm]	Discharge Coefficient(Cd)
3	5.38	0.94
7	5.38	0.95
9	5.38	0.92

For all cases, the cavitation sheet can be seen and the flow is choked. However, there is some differences in the flow rates. For the maximum discharge coefficient, the optimum angle for the outlet is 7 degrees.

5.2.2 Throat Length Investigation

In the validation case, throat length was zero. In general, the throat length is not desired for the design of the Venturi due to causing higher pressure loss. However, in the variable area Venturi case with zero throat length, occurrence of the cavitation is seen at very limited time. Therefore, in order to guarantee the occurrence of cavitation, there should be a throat length in the Venturi section.

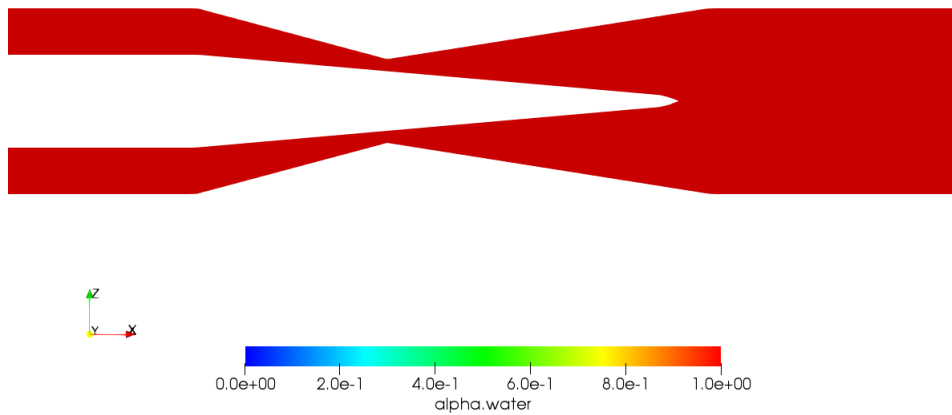


Figure 5.17: No Throat Length Case

5.2.3 Effect of Inlet/Outlet Pressure

Two sets of CFD analysis have been done in order to examine effect of the inlet and outlet pressures on the cavitating flow.

First, three different CFD analysis have been made on the flow through variable area Venturi. The aim is to observe the performance of the variable area cavitating Venturi with different inlet pressures. There is a graph related to these analyses in Figure 5.18.

When looking at the results of time-dependent analyses result, the flow oscillations are gradually decreasing. On the other hand, in the case of a fixed area cavitating Venturi, the oscillations are never damped out and they last. The time dependent mass flow rate results are compared for the three different cases in Figure 5.19.

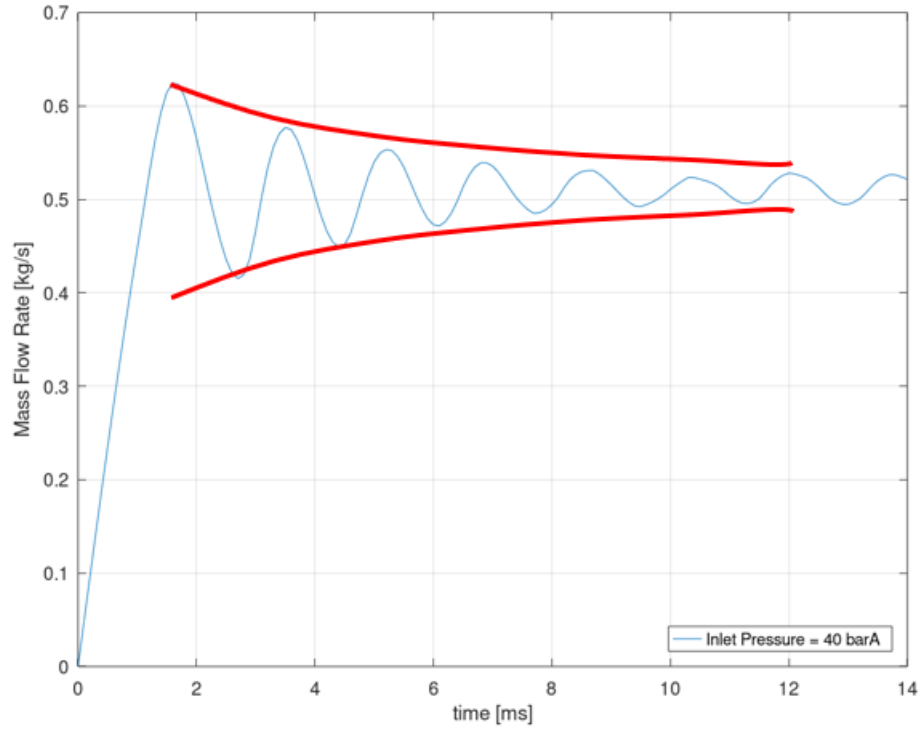


Figure 5.18: Mass Flow Rate vs. Time

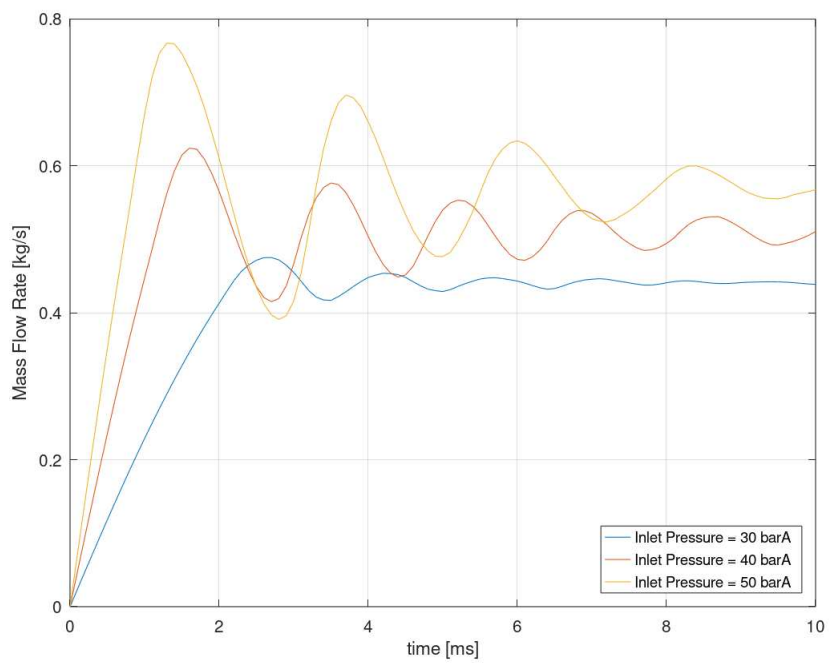


Figure 5.19: Mass Flow Rate Comparison for Different Inlet Pressure

The discharge coefficient versus the inlet pressure is given in the Figure 5.20.

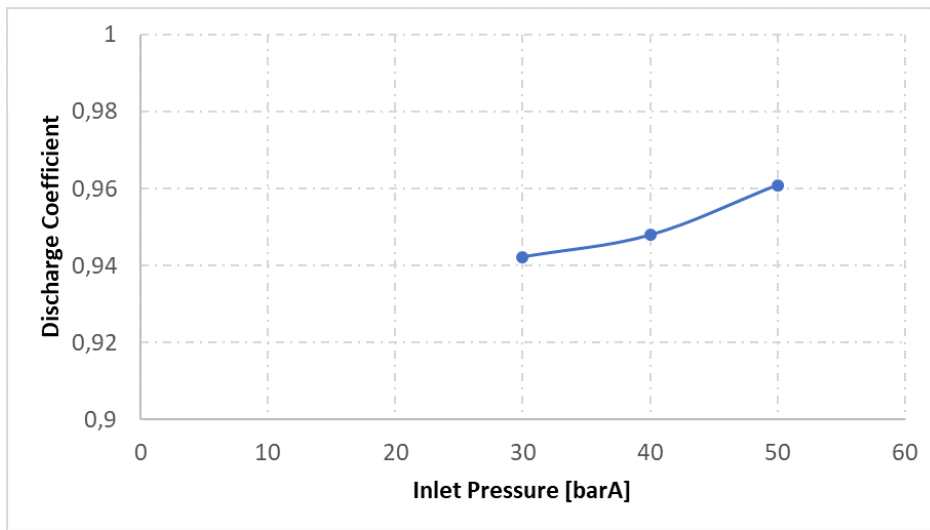


Figure 5.20: Discharge Coefficient vs Inlet Pressure

In order to check whether the flow rate depends on the downstream pressure or not, two simulations have been carried out with the same inlet pressure but different outlet pressure. For both case, it is seen that the flow rate does not change with outlet pressures. Therefore, the discharge coefficient is constant for both cases.

5.2.4 Summary of the CFD Simulations

All CFD simulations related to the variable area cavitating Venturi is summarized in Table 5.5.

The main difference between the simulations of the fixed area and the variable area Venturi's is the cavitation mechanism. In the fixed area Venturi case, the flow loses its energy after the throat region due to highly turbulent flow near the wall. As a result, the pressure value decreases and cavitation occurs near the wall.

On the contrary, in the variable area Venturi flow, flow separation does not exist. The cavitation occurs at the highest velocity region. Increasing of velocity causes enough static pressure loss in the Venturi flow so that cavitation can occur. Since there is no interaction of the highly turbulent flow and cavitation phenomena, the flow is more

stable.

Table 5.5: Summary of Simulations Conducted

Case	Stroke[mm]	Outlet Angle[deg]	σ	Cd	Re
1	4.38	3	2.98	0.94	10×10^4
2	5.38	3	2.98	0.94	12×10^4
3	6.38	3	2.98	0.92	14×10^4
4	7.38	3	2.98	0.91	16×10^4
5	5.38	3	1.98	0.94	12×10^4
6	5.38	3	2.4	0.94	12×10^4
7	5.38	3	2	0.95	14×10^4
8	5.38	3	1.66	0.96	16×10^4
9	5.38	7	2.98	0.95	12×10^4
10	5.38	9	2.98	0.92	12×10^4

CHAPTER 6

CONCLUSION&FUTURE WORK

In this work, the multi-phase flow through the Venturi is investigated both numerically and experimentally. The cavitating flow is simulated with OpenFoam software using Schnerr-Sauer cavitation model and k-omega SST turbulence model. In order to validate and verify the solver and the model, the fixed area cavitating Venturi has been taken as a validation case. Based on this verified solver and model, the design of the variable area Venturi has been realized. Then, the variable area cavitating Venturi performance has been obtained from the simulations.

In the experimental study, the Venturi flow is examined by flow visualization and measurement techniques. The test results have shown that the cavitation occurs when the inlet to outlet pressure ratios is below 0.8. The cavitation mechanism has been examined by using a high speed camera. It has been observed that cavitating flow is highly unsteady. The bubble formation and collapse can easily be seen during the tests. Using image process tools, this flow oscillation frequency has been tried to be determined. Flow oscillations are very critical for liquid propellant rocket engines since a frequency overlapping may result in combustion instability. Consequently, that may lead to a catastrophic failure.

The comparison of the test results and simulations conducted is one of the important aims of this study. The fixed area cavitating Venturi case is taken as a base for this comparison. In the overall, the CFD results show high coherence with the test results especially concerning the flow rates. There is approximately 4 % difference between the results. In addition, other main characteristics such as the cavitation length and the outlet pressure independency has been observed to be very consistent with the test results. On the other hand, the frequency of the flow instability cannot be estimated

accurately. Note that, the FFT results and image processing data are not completely comparable since there is a distance between the downstream pressure sensor location and the throat of the Venturi. Yet, the trend obtained from the simulations is the same with one obtained from the test results.

The oscillation behavior with the variable area Venturi flow differs from the one with the fixed area Venturi, which is one of the main findings of this study. The oscillation amplitudes in the variable area Venturi flow are getting damped as time passes. On the other hand, they never damp in the fixed area cavitating Venturi flow.

The variable area Venturi simulations have shown that the flow rate rises linearly with the pintle positions. The effects of the downstream and upstream pressures on the Venturi flow have been investigated. Since the pressure drop at a certain flow rate is a very key parameter for designing a Venturi for a liquid propellant rocket engine system, the discharge coefficient relation with different boundary conditions and geometrical dimensions has been studied. A higher discharge coefficient means a lower pressure drop at a certain flow rate. After investigations, the optimum outlet angle for the divergence part of the Venturi is found to be 7 degrees.

To sum up, the cavitating flow is simulated using with Schnerr-Sauer model. The design has been characterized in detail through the OpenFoam simulations. Although there are some deviations between the test and the simulation results, it is shown that the used OpenFoam solver has the ability to solve the multi-phase flow with acceptable accuracy. As mentioned before, Schnerr-Sauer relies on several assumptions to model cavitation. As a future work, a new extensive model can be developed to simulate multi-phase flow including a more accurate representation of bubble dynamics. Moreover, a more advanced turbulence model such as Large Eddy Simulation can be applied.

REFERENCES

- [1] Almeida, D., & Pagliuco, C. (2014). Development Status of the L75: A Brazilian Liquid Propellant Rocket Engine. *Journal Of Aerospace Technology And Management*, 6(4), 475-484. doi: 10.5028/jatm.v6i4.386
- [2] Solmaz, M., & Yazici, B. (2014). Numerical & Experimental Investigation of Cavitating Venturi Geometry on LOX Flows. 50Th AIAA/ASME/SAE/ASEE Joint Propulsion Conference. doi: 10.2514/6.2014-3997
- [3] Casiano, M., Hulka, J. and Yang, V. (2010). Liquid-Propellant Rocket Engine Throttling: A Comprehensive Review. *Journal of Propulsion and Power*, 26(5), pp.897-923.
- [4] Ghassemi, H., & Fasih, H. (2011). Application of small size cavitating venturi as flow controller and flow meter. *Flow Measurement And Instrumentation*, 22(5), 406-412. doi: 10.1016/j.flowmeasinst.2011.05.001
- [5] Abdulaziz, A. (2014). Performance and image analysis of a cavitating process in a small type venturi. *Experimental Thermal And Fluid Science*, 53, 40-48. doi: 10.1016/j.expthermflusci.2013.10.010
- [6] Mena, J., Ingle, M., Shirsat, V., & Choudhuri, A. (2015). An investigation of a cavitating venturi flow control feature in a cryogenic propellant delivery system. *Flow Measurement And Instrumentation*, 41, 97-103. doi: 10.1016/j.flowmeasinst.2014.09.008
- [7] HARVEY, D. (1970). Throttling venturi valves for liquid rocket engines. 6Th Propulsion Joint Specialist Conference. doi: 10.2514/6.1970-703
- [8] Tian, H., Zeng, P., Yu, N., & Cai, G. (2014). Application of variable area cavitating venturi as a dynamic flow controller. *Flow Measurement And Instrumentation*, 38, 21-26. doi: 10.1016/j.flowmeasinst.2014.05.012

- [9] Xu, C., Heister, S., & Field, R. (2002). Modeling Cavitating Venturi Flows. *Journal Of Propulsion And Power*, 18(6), 1227-1234. doi: 10.2514/2.6057
- [10] Kleinstreuer C. *Modern Fluid Dynamics*. Springer, 2010, ISBN 978-1-4020-8670-0.
- [11] Goncalves, E. (2011). Numerical study of unsteady turbulent cavitating flows. *European Journal Of Mechanics - B/Fluids*, 30(1), 26-40. doi: 10.1016/j.euromechflu.2010.08.002
- [12] Sauer, J., & Schnerr, G. (2001). Development of a New Cavitation Model based on Bubble Dynamics. *ZAMM - Journal Of Applied Mathematics And Mechanics*, 81(S3), 561-562. doi: 10.1002/zamm.20010811559
- [13] Fortes Patella, Regiane & Barre, Stephane & Reboud, Jean-Luc. (2006). Experiments and modelling of cavitating flows in Venturi. Part II: unsteady cavitation.
- [14] Zwart, Philip & Gerber, A.G. & Belamri, Thabet. (2004). A two-phase flow model for predicting cavitation dynamics. *Fifth International Conference on Multiphase Flow*.
- [15] Singhal, A., Athavale, M., Li, H., & Jiang, Y. (2002). Mathematical Basis and Validation of the Full Cavitation Model. *Journal Of Fluids Engineering*, 124(3), 617. doi: 10.1115/1.1486223
- [16] Brinkhorst, S., Lavante, E., & Wendt, G. (2015). Numerical investigation of cavitating Herschel Venturi-Tubes applied to liquid flow metering. *Flow Measurement And Instrumentation*, 43, 23-33. doi: 10.1016/j.flowmeasinst.2015.03.004
- [17] OpenFOAM - CFD Online Discussion Forums. (2019). Retrieved 21 August 2019, from <https://www.cfd-online.com/Forums/openfoam/>
- [18] Brennen, C. (1995). *Cavitation and bubble dynamics*. New York: Oxford Univ. Press.
- [19] Coutier-Delgosha, O., Fortes-Patella, R., & Reboud, J. (2002). Simulation of unsteady cavitation with a two-equation turbulence model including compressibility effects. *Journal Of Turbulence*, 3, N58. doi: 10.1088/1468-5248/3/1/058

- [20] J. Zhu, Y. Chen, D. Zhao and X. Zhang, "Extension of the Schnerr–Sauer model for cryogenic cavitation", *European Journal of Mechanics - B/Fluids*, vol. 52, pp. 1-10, 2015. Available: 10.1016/j.euromechflu.2015.01.008.
- [21] Cazzoli, G., Falfari, S., Bianchi, G., Forte, C., & Catellani, C. (2016). Assessment of the Cavitation Models Implemented in OpenFOAM Under DI-like Conditions. *Energy Procedia*, 101, 638-645. doi: 10.1016/j.egypro.2016.11.081
- [22] E. Roohi, M-R. Pendar, A. Rahimi, Simulation of Three-Dimensional Cavitation behind a Disk using Various Turbulence and Mass Transfer Models, *Appl. Math. Modelling* (2015), doi: [http://dx.doi.org/ 10.1016/j.apm.2015.06.002](http://dx.doi.org/10.1016/j.apm.2015.06.002)
- [23] Menter, F. (1994). Two-equation eddy-viscosity turbulence models for engineering applications. *AIAA Journal*, 32(8), 1598-1605. doi: 10.2514/3.12149
- [24] (2019) Retrieved 14 November 2019, from <https://www.swagelok.com>
- [25] (2019) Retrieved 14 November 2019, from <https://www.trafag.com>
- [26] Gentek Elektronik. (2019). Retrieved 14 November 2019, from <http://www.gentekelektronik.com.tr/>
- [27] SimScale - CFD, FEA, and Thermal Simulation in the Cloud | CAE. (2019). Retrieved 30 November 2019, from <https://www.simscale.com>